

The quasi-periodically oscillating precursor of a long gamma-ray burst from a binary neutron star merger

Shuo Xiao^{1,2}, Yan-Qiu Zhang^{1,2}, Zi-Pei Zhu^{3,4}, Shao-Lin Xiong^{1*}, He Gao^{5*}, Dong Xu^{3*}, Shuang-Nan Zhang^{1*}, Wen-Xi Peng¹, Xiao-Bo Li¹, Peng Zhang⁶, Fang-Jun Lu¹, Lin Lin⁵, Liang-Duan Liu⁷, Zhen Zhang¹, Ming-Yu Ge¹, You-Li Tuo¹, Wang-Chen Xue^{1,2}, Shao-Yu Fu³, Xing Liu^{3,8}, An Li⁵, Tian-Cong Wang⁵, Chao Zheng^{1,2}, Yue Wang¹, Shuai-Qing Jiang³, Jin-Da Li⁵, Jia-Cong Liu^{1,2}, Zhou-Jian Cao⁵, Ce Cai^{1,2}, Qi-Bin Yi^{1,9}, Yi Zhao^{1,5}, Sheng-Lun Xie^{1,7}, Cheng-Kui Li¹, Qi Luo^{1,2}, Jin-Yuan Liao¹, Li-Ming Song¹, Shu Zhang¹, Jin-Lu Qu¹, Cong-Zhan Liu¹, Xu-Fang Li¹, Yu-Peng Xu¹, Ti-Pei Li^{1,2,10}

¹Key Laboratory of Particle Astrophysics, Institute of High Energy Physics, Chinese Academy of Sciences, 19B Yuquan Road, Beijing 100049, China

²University of Chinese Academy of Sciences, Chinese Academy of Sciences, Beijing 100049, China

³Key Laboratory of Space Astronomy and Technology, National Astronomical Observatories, Chinese Academy of Sciences, Beijing 100012, China

⁴Department of Astronomy, School of Physics, Huazhong University of Science and Technology, Wuhan 430074, China

⁵Department of Astronomy, Beijing Normal University, Beijing 100875, China

⁶College of Science, China Three Gorges University, Yichang 443002, China

⁷Department of Physics, Central China Normal University, Wuhan 430079, China

⁸Key Laboratory of Cosmic Rays, Ministry of Education, Tibet University, Lhasa, Tibet 850000, China

⁹School of Physics and Optoelectronics, Xiangtan University, Yuhu District, Xiangtan, Hunan, 411105, China

¹⁰Department of Astronomy, Tsinghua University, Beijing 100084, China

The milestone of GW 170817-GRB 170817A-AT 2017gfo¹ has shown that gravitational wave (GW) is produced during the merger of neutron star-neutron star/black hole and that in electromagnetic (EM) wave a gamma-ray burst (GRB) and a kilonovae (KN) are generated in sequence after the merger. Observationally, however, EM property during a merger is still unclear. Here we report a peculiar precursor in a KN-associated long GRB 211211A. The duration of the precursor is ~ 0.2 s, and the waiting time between the precursor and the main emission (ME) of the burst is ~ 1 s, which is about the same as the time interval between GW 170817 and GRB 170817A. Quasi-Periodic Oscillations (QPO) with frequency ~ 22 Hz (at $> 5\sigma$ significance) are found throughout the precursor, the first detection of periodic signals from any *bona fide* GRBs. This indicates most likely that a magnetar participated in the merger, and the precursor might be produced due to a catastrophic flare accompanying with torsional or crustal oscillations of the magnetar. The strong seed magnetic field of $\sim 10^{14-15}$ G at the surface of the magnetar may also account for the prolonged duration of GRB 211211A. However, it is a challenge to reconcile the rather short lifetime of a magnetar

² with the rather long spiraling time of a binary neutron star system only by gravitational wave radiation before merger.

GRB 211211A was detected at 2021-12-11 13:09:59.651 (UTC, denoted as T0) by *Fermi*/GBM³, *Swift*/BAT⁴ and *Insight*-HXMT/HE⁵. The full burst lightcurve can be divided into three emission episodes: a precursor (PRE) with duration of ~ 0.2 s in Fast Rising Exponential Decay (FRED) shape (as shown in Figure. 1), a ~ 8 s spiky hard main emission (ME), and a soft long extended emission (EE) up to $>\sim 50$ s³. This burst has a duration of $T_{90} \sim 34.3$ s in 10-1000 keV by *Fermi*/GBM³. From spectral analysis with *Fermi*/GBM and *Insight*-HXMT data, a significant spectral evolution is observed throughout the burst (Extended Data Table. 1), with the full burst time-averaged peak energy of $E_{\text{peak}} \sim 1.2$ MeV.

Optical follow-ups at the Nanshan/NEXT 0.6-m telescope localised the burst in a bright ($r = 19.5$) galaxy SDSS J140910.47+275320.8 (Extended Data Figure. 1) with a spectroscopic redshift of $z = 0.076$ reported at the Nordic Optical Telescope⁶. The offset between the burst and the nucleus of the galaxy is 5.11 ± 0.23 arcsec (corresponding to 7.61 ± 0.34 kpc in projection), indicating a very small probability of chance coincidence of 1.1%⁷. At $z = 0.076$, the isotropic equivalent energies E_{iso} are 7.7×10^{48} erg, 5.3×10^{51} erg and 2.2×10^{51} erg for PRE, ME and EE, respectively.

Besides the relatively large offset, other observational indicators (Figure. 2) also put GRB 211211A into the binary merger burst category (Type I) rather than the collapsar burst (Type II)⁸. In the $T_{90} - E_{\text{peak}}$ diagram, the probability as a merger burst is as high as 83.4% for the ME while only 2.2% for the full burst, i.e., PRE+ME+EE. In the $E_{\text{iso}} - E_{\text{peak}}$ (the so-called Amati correlation⁹) diagram, the PRE, the ME, and the full burst lie in the merger population while the EE shifts to the transitional area of the two populations to some extent. In the Spectral Lag - Isotropic equivalent luminosity $L_{\text{ag}} - L_{\text{iso}}$ ¹⁰ diagram, the burst is well-placed in the merger population. In addition, the small minimum variability timescale, $\Delta t_{\text{min}} \sim 10$ ms (Sec. 8 in **Methods**), is also consistent with the merger origin.

We monitored the optical counterpart of GRB 211211A for more than two weeks. Placing prototype GRB-associated broad-lined Type Ic supernovae (SNe Ic-BL) such as SN 1998bw, SN 2006aj, and SN 2010bh at $z = 0.076$, our late optical upper limits completely rule out any SN Ic-BL association (Extended Data Figure. 2). Together with public X-ray and optical/near-infrared data (Extended Data Table. 2), we fitted the counterpart with the standard forward shock afterglow model, and obtained a half-opening angle of $\sim 2.9^\circ$ for the GRB outflow jet (Extended Data Table. 3).

Interestingly, there exists an excess in optical/near-infrared after the standard afterglow subtraction. The multi-band lightcurves of the excess are quite similar to that of the prototype kilonova (KN), AT 2017gfo in GW 170817¹¹. We fitted the afterglow-subtracted data with the numerical two-component KN model, and obtained $M_{\text{ej},1} \sim 0.013 M_\odot$, $V_{\text{ej},1} \sim 0.33c$ for the relatively blue component and

$M_{\text{ej},2} \sim 0.037 M_{\odot}$, $V_{\text{ej},2} \sim 0.30c$ for the relatively red component, respectively.

No accompanied SN and detection of a AT 2017gfo-like KN ^{12,13} (Sec. 9 in **Methods**), in combination with specific positions in the above correlation diagrams, confirm that GRB 211211A is from a neutron star (NS)-neutron star/black hole (BH) merger, especially its moderate-sized blue component suggesting the burst more likely from a binary NS merger.

The precursor of GRB 211211A is identified with Bayesian Blocks (BB) algorithm ¹⁴, Li-Ma formula ¹⁵ and statistical tests based on χ^2 statistic (Sec. 2 in **Methods**). The precursor is well separated with the main burst by a quiescence period of about 1 s, during which the lightcurve decreased to the background. The significance of the ‘possible weak signal’ in T_{wt} using the Li-Ma formula is 0.5σ , which is consistent with background fluctuation. We note that this is the only quiescence time during the entire burst. Interestingly, this precursor follows well the relation between the waiting time and precursor duration of SGRBs (see Figure. 2), lending additional support to the merger origin despite of the prolonged ME of this burst.

With the BB algorithm, we calculate the duration (in 8-200 keV) of the precursor as $T_{\text{pre}} \sim 0.19$ s (T0-0.017 to T0+0.17 s) of GBM, ~ 0.2 s of BAT, ~ 0.1 s of HXMT/HE, the waiting time between the precursor and the ME as $T_{\text{wt}} \sim 0.93$ s (T0+0.17 to T0+1.10 s), ~ 0.88 s (BAT) and ~ 1.28 s (HXMT/HE) (Sec. 2 in **Methods**).

The overall shape of the precursor lightcurve can be fitted well with the FRED model, with the rising time of $8.0^{+2.4}_{-2.2}$ ms, $10.0^{+2.1}_{-2.2}$ ms and $10.4^{+12.2}_{-6.4}$ ms by Fermi/GBM, Swift/BAT and HXMT/HE data respectively, while the decay time is $84.0^{+10.8}_{-10.7}$ ms, $99.2^{+8.0}_{-8.4}$ ms and $43.1^{+12.0}_{-12.3}$ ms (see Extended Data Table. 7).

The spectrum of precursor could be well fit with a cutoff power-law (CPL) model, without thermal component. The average flux of the precursor is $1.8^{+0.1}_{-0.9} \times 10^{-6}$ erg/cm²/s between 10 keV and 1000 keV. The time-averaged isotropic luminosity in the same energy range is $2.6^{+0.1}_{-1.3} \times 10^{49}$ erg/s, the 64-ms peak isotropic luminosity is $7.4^{+0.8}_{-0.7} \times 10^{49}$ erg/s, and the total energy released is $7.7^{+0.4}_{-1.7} \times 10^{48}$ erg, considering the distance of 346.1 Mpc. The spectrum of the precursor is softer than both ME and EE. The E_p evolution of precursor has a “hard to soft” pattern. The spectral lag of the precursor between 200-250 keV and 100-150 keV at rest frame is -7.4 ± 20.5 ms, consistent with zero.

Most interestingly, we find that there are several regularly-spaced pulses superimposed on the FRED trend in the precursor lightcurves of Fermi/GBM and Swift/BAT (see Extended Data Figure. 6), which hints possible Quasi-Periodic Oscillations (QPO) (Figure. 1) from T0-0.1 s to T0+0.3 s (see Figure. 3). We therefore use several methods to search for the frequency and to estimate the significance of the possible QPOs, using the FRED-subtracted lightcurves to minimize the effect of the overall precursor profile on our analyses.

First, we employ one of the most widely used methods, the Weighted Wavelet Z-transform (WWZ) ¹⁶, to obtain the power spectra of GBM and BAT light-curves. A strong peak at 22^{+3}_{-2} Hz (GBM) and 22^{+3}_{-1} Hz (BAT) (with period cycle of 45^{+5}_{-4} ms and 45^{+5}_{-2} ms) is detected in WWZ powers (Figure. 3). The uncertainty of the QPO frequency is the full width at half maximum of the peak. To estimate the confidence level more robustly, we choose the time from -0.1 s to 0.3 s and generate 2×10^4 artificial light-curves using the REDFIT method ¹⁷. The simulation results show that the signal has 3.0σ and 2.0σ false-alarm level for GBM and BAT at ~ 22 Hz, respectively (Extended Data Figure. 7); the joint significance is 4.0σ , given that the GBM and BAT data are independent.

Then, we perform Fast Fourier analyses to generate power spectra (Sec. 6 in **Methods**) on the GBM and BAT lightcurves, respectively. The Leahy normalized power of the lightcurves of GBM and BAT with FRED subtracted are shown in Figure. 3 (Sec. 6 in **Methods**). The QPO signals at frequency about 22.5 Hz are found with significance of 4.1σ (GBM) and 3.0σ (BAT), respectively; the joint significance is 5.4σ .

Several other methods, including the auto-correlation analysis, the Lomb-Scargle Periodogram (LSP) ¹⁸, and the Z^2 method, harmonic=1 (Sec. 6 in **Methods**) are also used to analyze the QPO properties. They all give the frequency around 22 Hz and with comparable or even higher detection significance (Sec. 6 in **Methods**). It is worthy to note that, with the same methods, no periodic signal is found in the ME and EE of the GRB.

Despite of many attempts to search QPOs in GRBs, there is no conclusive result reported before the present work. By contrast, QPOs of 10's Hz to 1000's Hz have been found in several soft gamma-ray repeaters (SGRs), e.g. Giant Flares (GF) of SGR 1806–20 ¹⁹ and SGR 1900+14 ²⁰, and SGR J1935+2154 burst associated with a Fast Radio Burst (FRB 200428) ²¹. They are usually interpreted as the torsional oscillations ^{22,23} or the crust oscillations ²⁴ of a neutron star (NS) with extremely high magnetic field of $\sim 10^{14-15}$ G, i.e. magnetar. From this point of view, the 22 Hz QPO signal reported here may not be a knotty problem, as long as a magnetar is involved in the progenitor system. The flares and bursts from magnetars are generally considered to be nearly isotropic, or at least not obviously beamed. It is thus interesting to note that the precursor's total energy output $E_{\text{iso}} \sim 7.7 \times 10^{48}$ erg (Extended Data Table. 3) is comparable to the jet-corrected energies E_γ for ME and EE, which are 6.6×10^{48} erg and 2.8×10^{48} erg, respectively. Therefore the precursor is energetically very important for this event.

Considering a binary NS merger for GRB 211211A, due to the shielding of ejected material, it is difficult to produce strong non-thermal emission with QPO in the initial stage of post-merger phase. Besides, the waiting time between the precursor and main burst (~ 1 s) is consistent with the time interval between the binary neutron star merger and the GRB in GW 170817 ¹. We therefore suggest that most likely a magnetar participated in the merger, and this precursor was produced due to a catastrophic flare accompanying with torsional or crustal oscillations of the magnetar.

The flare might be produced ~ 0.2 s before the coalescence when the orbital period (P_b) is ~ 8 ms and the orbital distance is ~ 80 km (Sec. 10 in **Methods**). At this distance, the magnetar's torsional or crustal oscillations are barely affected by the tidal disruption. On the other hand, considering the rising time of 8 ms, the emission region of the precursor would be ≥ 2400 km, which is way beyond the common magnetosphere's light cylinder of the binary system ($2\pi c/P_b \sim 380$ km). For these reasons, it is not surprising that a stable oscillation period of radiation could be maintained during the violent orbital evolution of the binary system in the final stage of merging. An alternative model to interpret the precursor is the magnetospheric interactions in the NS binary. In this scenario, it is also necessary to introduce a magnetar with surface magnetic field $\sim 10^{14-15}$ G in the final merging phase (Sec. 11 in **Methods**), but the QPO feature is rather difficult to produce. A difficulty, however, is to reconcile the rather short lifetime of a magnetar² with the rather long spiraling time of a binary NS system only by gravitational wave radiation before merger.

Numerical relativity simulations show that for the merger of binary highly magnetized neutron stars, central engine of GRBs would be modeled by a magnetized accretion torus with saturated strength²⁵. With the magnetic barrier effect, radial angular momentum transfer may significantly prolong the lifetime of the accretion process, so as the GRB duration^{26,27}. On the other hand, it is shown that the gravitational waveforms of magnetized and unmagnetized NS binaries could be well distinguished as long as the NS magnetic field is strong enough²⁸. Future multi-messenger detections could help to confirm whether the progenitor of GRB 211211A-like bursts really contains a highly magnetized NS and unveil the physical origin of the precursor and its intriguing QPO behavior.

Acknowledgements This work made use of the data from the *Insight-HXMT*, *Fermi* and *Swift*. This work is supported by the National Key R&D Program of China (2021YFA0718500) and the National Natural Science Foundation of China (Projects: 12061131007, 12021003). S.-L. X. acknowledges supports by the Strategic Priority Research Program on Space Science (Grant No. XDA15052700, XDB23040400) of the Chinese Academy of Sciences (CAS). D.X. acknowledges the support by the Strategic Priority Research Program “Multi-wavelength Gravitational Wave Universe” of the CAS (No. XDB23000000) and the science research grants from the China Manned Space Project with NO. CMS-CSST-2021-A13, CMS-CSST-2021-B11. We thank Xing Gao for kind help of the Nanshan/NEXT observations. We thank Bing Zhang and BinBin Zhang for helpful discussions. We acknowledge the support of the staff of the Xinglong 2.16m telescope. This work was also partially supported by the Open Project Program of the Key Laboratory of Optical Astronomy, National Astronomical Observatories, Chinese Academy of Sciences.

Correspondence Correspondence and requests for materials should be addressed to (S.-L. X., H. G., D. X. and S.-N. Z., email: xiongs1@ihep.ac.cn, gaohe@bnu.edu.cn, dxu@nao.cas.cn, zhangsn@ihep.ac.cn).

Author Contributions S.-L.X., H.G. and D.X. initiated this project. S.-L.X led the high energy data analysis. H.G. led the theory interpretation. D.X. led the optical follow-ups and relevant data analysis. S.-N.Z. led the QPO analysis and the organization of the manuscript. S.X. is the main contributor to the high energy data analysis and participated in paper writing. Y.-Q.Z., S.-L.X., S.-N.Z, F.-J.L., W.-X.P., X.-B.L., P.Z., Y.-L.T., W.-C.X., H.G., M.-Y.G., C.Z., Y.W., J.-C.L. participated in the high energy data analysis. D.X., Z.-P.Z., S.-Y.F., X.L., S.-Q.J., J.-D.L., H.G. participated in the optical observations and data analysis. H.G., S.-N.Z., A.L., T.-C.W., L.-D.L., F.-J.L., S.-L.X., D.X., Z.Z., L.L., S.X., Z.-J.C. participated in the theory interpretation and discussion. S.-N.Z., S.-L.X., H.G., D.X., F.-J.L., Y.-Q.Z., Z.-P.Z., W.-X.P., X.-B.L., P.Z., W.-C.X., C.Z., L.-D.L., Z.Z., L.L., participated in the writing and editing of the paper. All other authors participated in the discussion and contributed to the *Insight-HXMT* GRB research which is important for this work.

Competing Interests The authors declare no competing interests.

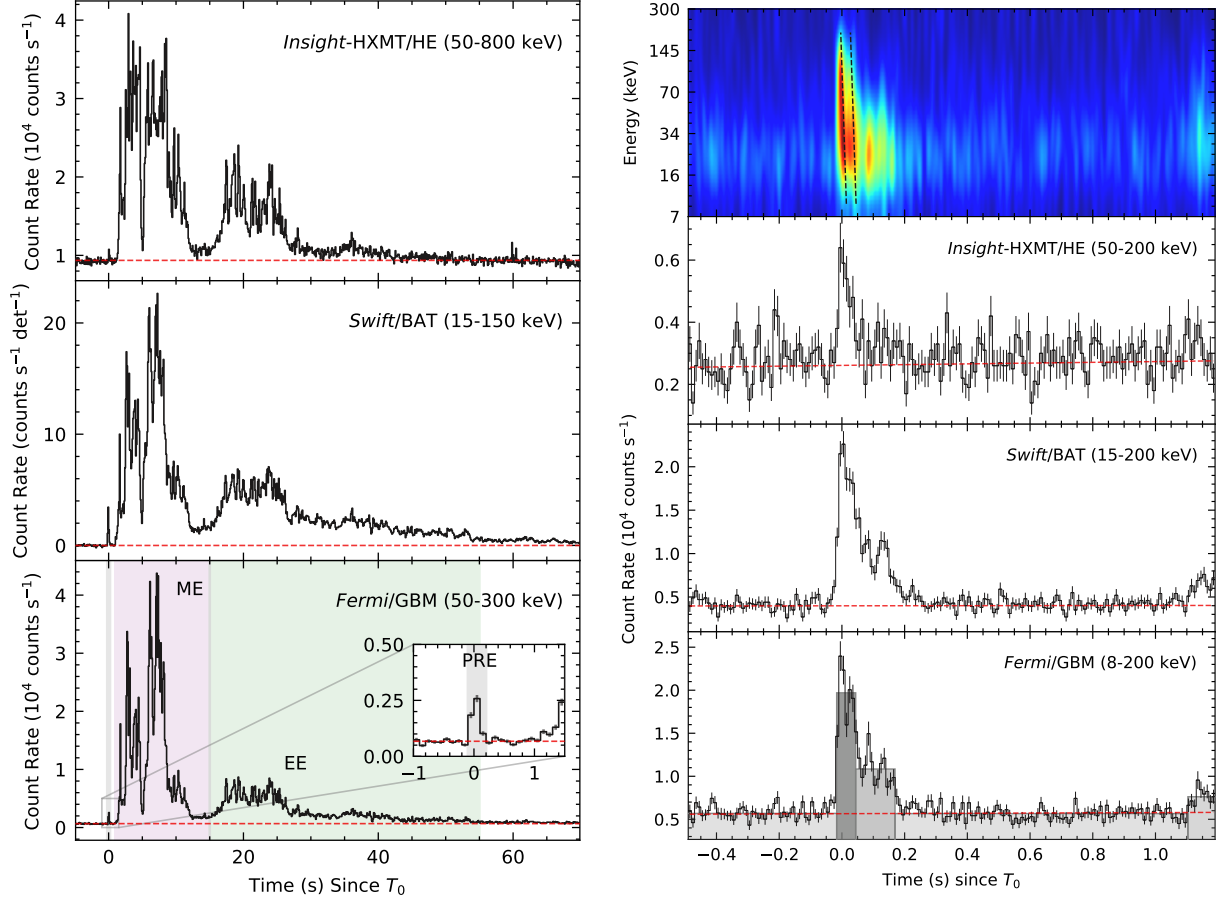


Figure. 1: **Left panels:** lightcurves and the T_{90} calculation of GRB 211211A. The top panel is the summed *Insight*-HXMT/HE lightcurve for all the 18 detectors in 50-800 keV energy range (the incident energy greater than ~ 100 keV). The second panel is the summed *Swift*/BAT mask-weighted and background-subtracted lightcurve for 15-500 keV energy range. The third panel is the summed *Fermi*/GBM lightcurve for n2 and na in 50-300 energy range. **Right panels:** lightcurves of the precursor observed by *Insight*-HXMT/HE, *Swift*/BAT and *Fermi*/GBM, the time bin is 10 ms. The light travel time difference has been corrected. The T_{pre} and T_{wt} at 8-200 keV band are about 0.19 s and 0.93 s, respectively. The shaded bars in the bottom panel show the lightcurve structure obtained by BB algorithm. The black dashed lines in the top panel represent logarithmic spectral lag behavior on time-energy domain, $t(E) = 0.006 \ln(E) + C$.

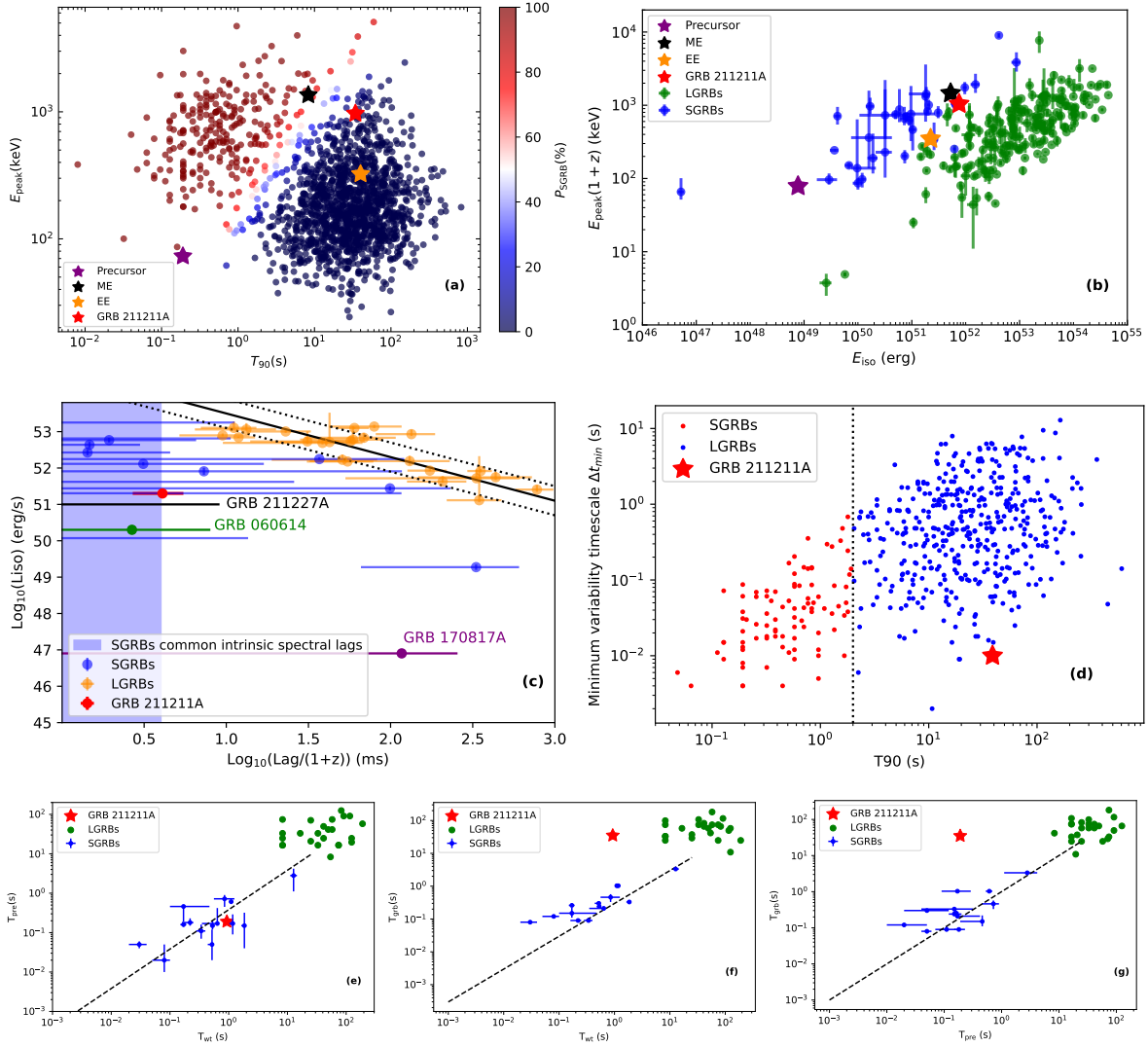


Figure 2: **(a)** T_{90} v.s. E_{peak} . The precursor, ME, EE and full burst of GRB 211211A are marked with purple, black, orange and red stars, respectively. **(b)** E_{iso} v.s. $E_{\text{peak}}(1+z)$. The GRB sample is mainly collected from Fermi GBM Burst Catalog⁴⁷, Konus-Wind Burst Catalog⁴⁶, and the literature^{48–53}. **(c)** Lag v.s. L_{iso} . The GRB sample is collected from the literature^{58,61–63,74}, and GRB 211211A is highlighted by a red error bar (1σ). The blue shaded region represents the common intrinsic spectral lags (3σ) calculated from 46 SGRBs with redshift measurements⁶¹. **(d)** T_{90} v.s. Minimum Variability Timescale Δt_{min} . The samples of SGRBs (red dots) and LGRBs (blue dots) are from the literature⁷⁶. **(e)** The waiting time T_{wt} v.s. the full duration of the precursor emission T_{pre} . **(f)** T_{wt} v.s. the full duration of the GRB T_{grb} . **(g)** T_{pre} v.s. T_{grb} . The GRB sample is obtained from the literature^{31,32}. $T_{\text{pre}} \approx 0.38 T_{\text{wt}}$ is obtained by fitting SGRBs.

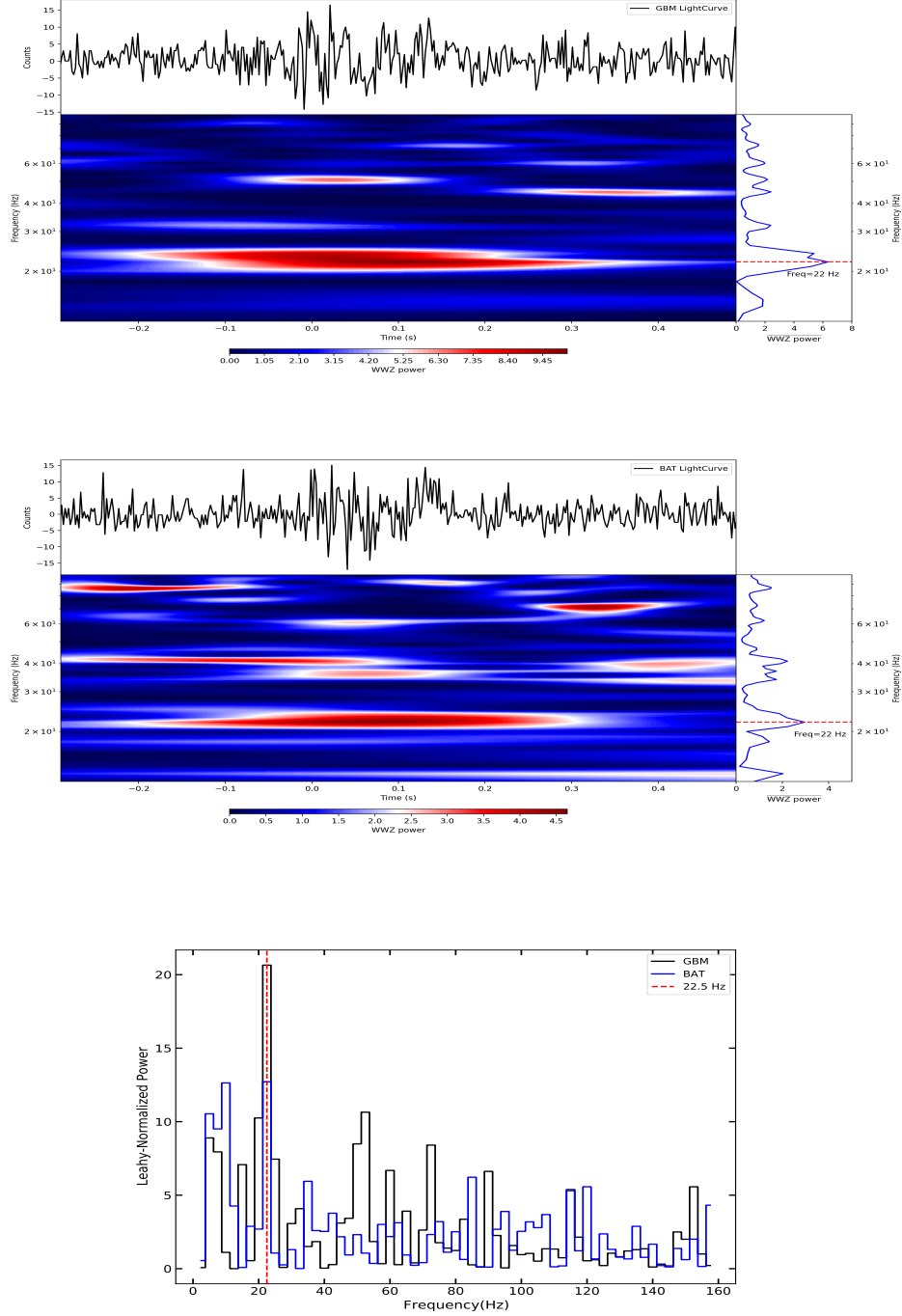


Figure. 3: **Top and middle:** GBM and BAT FRED-subtracted precursor lightcurves in 8-200 keV and the 2D plane contour plot of WWZ power. The blue solid lines represent the time-averaged WWZ power respectively. The red dash lines represent the QPO frequency. The significance for GBM and BAT are 3.0σ and 2.0σ , respectively; the joint significance is 4.0σ , since the GBM data and the BAT data are independent. **Bottom panel:** The Leahy normalized power of *Fermi*/GBM and *Swift*/BAT with the FRED-model subtracted lightcurve. The significance for GBM and BAT are 4.1σ and 3.0σ , respectively; the joint significance is 5.4σ .

1. Abbott, B. P. et al. Multi-messenger Observations of a Binary Neutron Star Merger. The Astrophysical Journal Letters **848**, L12 (2017).
2. Kaspi, V. M. & Beloborodov, A. M. Magnetars. Annual Review of Astronomy and Astrophysics **55**, 261–301 (2017).
3. Mangan, J., Dunwoody, R., Meegan, C., Team, F. G. et al. Grb 211211a: Fermi gbm observation. GRB Coordinates Network **31210**, 1 (2021).
4. D’Ai, A. et al. Grb 211211a: Swift detection of a bright burst. GRB Coordinates Network **31202**, 1 (2021).
5. Zhang, Y. et al. Grb 211211a: Insight-hxmt/he detection. GRB Coordinates Network **31236**, 1 (2021).
6. Malesani, D. B. et al. GRB 211211A: NOT optical spectroscopy. GRB Coordinates Network **31221**, 1 (2021).
7. Bloom, J. S., Kulkarni, S. R. & Djorgovski, S. G. The Observed Offset Distribution of Gamma-Ray Bursts from Their Host Galaxies: A Robust Clue to the Nature of the Progenitors. The Astronomical Journal **123**, 1111–1148 (2002).
8. Zhang, B. et al. Making a Short Gamma-Ray Burst from a Long One: Implications for the Nature of GRB 060614. The Astronomical Journal **655**, L25–L28 (2007).
9. Amati, L. et al. Intrinsic spectra and energetics of BeppoSAX Gamma-Ray Bursts with known redshifts. Astronomy & Astrophysics **390**, 81–89 (2002).
10. Norris, J. P., Marani, G. F. & Bonnell, J. T. Connection between Energy-dependent Lags and Peak Luminosity in Gamma-Ray Bursts. The Astrophysical Journal **534**, 248–257 (2000).
11. Villar, V. A. et al. The Combined Ultraviolet, Optical, and Near-infrared lightcurves of the Kilonova Associated with the Binary Neutron Star Merger GW170817: Unified Data Set, Analytic Models, and Physical Implications. The Astrophysical Journal Letters **851**, L21 (2017).
12. Rastinejad, J. et al. A kilonova following a long-duration gamma-ray burst at 350 mpc. arXiv preprint arXiv:2204.10864 (2022).
13. Yang, J. et al. A peculiarly long-duration gamma-ray burst from binary neutron star merger. arXiv preprint arXiv:2204.12771 (2022).
14. Scargle, J. D., Norris, J. P., Jackson, B. & Chiang, J. Studies in astronomical time series analysis. vi. bayesian block representations. The Astrophysical Journal **764**, 167 (2013).
15. Li, T.-P. & Ma, Y.-Q. Analysis methods for results in gamma-ray astronomy. The Astrophysical Journal **272**, 317–324 (1983).

16. Foster, G. Wavelets for period analysis of unevenly sampled time series. The Astronomical Journal **112**, 1709–1729 (1996).
17. Schulz, M. & Mudelsee, M. Redfit: estimating red-noise spectra directly from unevenly spaced paleoclimatic time series. Computers & Geosciences **28**, 421–426 (2002).
18. Zechmeister, M. & Kürster, M. The generalised lomb-scargle periodogram. a new formalism for the floating-mean and keplerian periodograms. Physics **496**, 577–584 (2009).
19. Watts, A. L. & Strohmayer, T. E. Detection with rhesi of high-frequency x-ray oscillations in the tail of the 2004 hyperflare from sgr 1806–20. The Astrophysical Journal **637**, L117 (2006).
20. Strohmayer, T. E. & Watts, A. L. Discovery of fast x-ray oscillations during the 1998 giant flare from sgr 1900+ 14. The Astrophysical Journal **632**, L111 (2005).
21. Li, X. et al. Quasi-periodic oscillations of the x-ray burst from the magnetar sgr j1935+ 2154 and associated with the fast radio burst frb 200428. arXiv preprint arXiv:2204.03253 (2022).
22. Link, B. & Van Eysden, C. A. Torsional oscillations of a magnetar with a tangled magnetic field. The Astrophysical Journal Letters **823**, L1 (2016).
23. Gabler, M., Cerdá-Durán, P., Font, J. A., Müller, E. & Stergioulas, N. Magneto-elastic torsional oscillations of magnetars. In Journal of Physics: Conference Series, vol. 283, 012013 (IOP Publishing, 2011).
24. Samuelsson, L. & Andersson, N. Neutron star asteroseismology. axial crust oscillations in the cowling approximation. Monthly Notices of the Royal Astronomical Society **374**, 256–268 (2007).
25. Kiuchi, K., Kyutoku, K., Sekiguchi, Y., Shibata, M. & Wada, T. High resolution numerical relativity simulations for the merger of binary magnetized neutron stars. Physical Review D **90**, 041502 (2014).
26. Proga, D. & Zhang, B. The late time evolution of gamma-ray bursts: ending hyperaccretion and producing flares. Monthly Notices of the Royal Astronomical Society: Letters **370**, L61–L65 (2006).
27. Liu, T. et al. Radial Angular Momentum Transfer and Magnetic Barrier for Short-type Gamma-Ray-burst Central Engine Activity. The Astrophysical Journal **760**, 63 (2012).
28. Giacomazzo, B., Rezzolla, L. & Baiotti, L. Can magnetic fields be detected during the inspiral of binary neutron stars? Monthly Notices of the Royal Astronomical Society: Letters **399**, L164–L168 (2009). URL <https://doi.org/10.1111/j.1745-3933.2009.00745.x>.

Methods

1 Lightcurve and T_{90} .

We estimate T_{90} , which is the time during which 90% of the 50-300 keV event photons were collected, using detectors NaI 2 (n2) and 10 (na) of GBM with angle between the detector normal to GRB 211211A less than 60 degrees to obtain as 38.8 ± 0.4 s. We also calculated the T_{90} of the main emission, which is ~ 8 s. Also, the T_{90} of HXMT/HE is 32.5 ± 1.0 s. It is worth noting that the measured duration of GRB can vary among different instruments and energy ranges²⁹. Note that this burst is so bright that the main emission (T0+1:T0+9 s) saturated HE³⁰.

2 Precursor identification.

A precursor should satisfy the following requirements³¹: (1) the first pulse in the lightcurve; (2) the peak count rate is lower than that of the main pulse; (3) the count rate during the waiting time period, i.e., the time interval between the precursor and the main pulse is consistent with the background level; (4) a significance enough to be identified as signal.

Bayesian Block (BB) algorithm¹⁴ is widely used to identify the precursor^{31,32} of GRBs. Here we employed the same technique to confirm the existence of precursor of GRB 211211A. Extended Data Table. 4 lists the time windows of the precursor and waiting time obtained from BB algorithm. The pulse near T_0 clearly satisfies the first two and last criterion, as shown in Figure. 1.

For the third criterion, two statistical schemes were adopted to test if the lightcurve of the waiting time period is background. We first calculated the significance of the ‘possible weak signal’ within T_{wt} by Li-Ma formula¹⁵, which is defined as

$$S = \sqrt{2} \left\{ n \log \left[\frac{\alpha + 1}{\alpha} \left(\frac{n}{n + b} \right) \right] + b \log \left[(\alpha + 1) \frac{b}{n + b} \right] \right\}^{1/2}, \quad (1)$$

where n is the counts of a certain time t_{on} within which a suspected source exists, b is the measured background counts in a time interval t_{off} , and α is the ratio of the on-source time to the off-source time t_{on}/t_{off} . After choosing the quiescent period determined by Bayesian Block algorithm as t_{on} and $T_0 - 1.1$ to $T_0 - 0.1$ s as t_{off} , the Li-Ma formula gave a significance of 0.5σ for GBM and of 1.7σ for BAT, which are consistent with background fluctuation.

To further investigate the lightcurve behavior during the waiting time period, we fit the $T_0 - 1.1$ to $T_0 - 0.1$ s background lightcurves of three instruments with a first-order polynomial, and interpolate over $T_0 - 0.5$ to $T_0 + 1.25$ s, then the estimate of background rate is obtained. The significance of a potential signal relative to background noise level can be calculated through weighting the difference between the lightcurve and estimate background, this quantity is commonly referred to as χ . As shown in Extended Data Figure. 3, χ is randomly distributed

around zero within the waiting time period. We apply the χ^2 and Anderson–Darling test to examine the overall fluctuation and normality of χ within this period, respectively. As shown in Extended Data Table. 4, the large p-value of χ^2 test implies the overall fluctuation of χ is consistent with background, and the high significance of Anderson–Darling test shows the well normality of χ , i.e., the lightcurves behave like background. All the statistical evidence indicates the quiescent period exists no significant signal, thus these pulses near T_0 should be identified as a precursor.

Furthermore, the precursor follows well the $T_{\text{pre}} \approx 0.38 T_{\text{wt}}$ relation for SGRBs.

3 $T_{\text{wt}} - T_{\text{pre}} - T_{\text{GRB}}$ correlation.

Precursors are detected in about 10% detected by Swift and most are , and found no significant difference between the precursor emission and the main emission episode, suggesting that precursors are directly related to the central engine activities share the same physical origin with the prompt episode ³². A few SGRBs, about 2.7% detected by *Swift*/BAT and *Fermi*/GBM ^{31,33}, also have precursor emission. The thermal precursors of SGRBs may be caused by the shock breakout or the photospheric radiation of a fireball launched after the merger, and nonthermal precursors may be explained by magnetospheric interaction between two neutron stars prior to the merger ^{36,38}. Wang et al. ³¹ find that the durations of the main SGRB emission (T_{GRB}) and the precursor emission (T_{pre}), as well as the waiting time (T_{wt}) in between, are roughly comparable to each other, with $T_{\text{wt}} \simeq 2.8 T_{90}^{1.2}$ approximately satisfied for most cases. However, it is obvious that the precursor reported here does not satisfy the $T_{\text{wt}} \simeq 2.8 T_{90}^{1.2}$ and $T_{\text{pre}} \sim T_{90}$ relations in ³¹ due to its long duration.

4 Fitting the precursor lightcurve with the FRED model.

The shape of most GRB pulses are typically asymmetric with a fast rise and a slow decay. Several empirical functions have been proposed to fit the pulse shape. A common form is called the fast-rising exponential decay (FRED)³⁴ as follows

$$I(t) = \begin{cases} A \exp \left[- \left(\frac{|t-t_{\text{max}}|}{t_r} \right)^\nu \right] + B, & t < t_{\text{max}} \\ A \exp \left[- \left(\frac{|t-t_{\text{max}}|}{t_d} \right)^\nu \right] + B, & t > t_{\text{max}} \end{cases} \quad (2)$$

, where A is the normalization parameter, t_{max} the peak time, t_r and t_d the rise and decay time constants, ν the sharpness of the pulse, and B the background for each time bin. The precursor data of GRB 211211A detected by *Fermi*/GBM, *Swift*/BAT and *Insight*-HXMT/HE was binned to 10 ms in our lightcurve fitting. The energy band is selected range from 8 to 200 keV for *Fermi*/GBM, from 15 to 200 keV for *Swift*/BAT, from 50 to 200 keV for *Insight*-HXMT/HE. The Bayesian inference method is employed in the LC fitting with assuming the prior as the uniform distribution.

The parameters of the lightcurve fitting with FRED model are shown in Extended Data Table. 7 with the confidence level of 68% and Extended Data Figure. 6. We noticed that multiple pulses are superimposed on the FRED curve which most notable in *Fermi*/GBM and *Swift*/BAT lightcurve, suspected as a periodic pulse.

5 Spectral fitting

Spectrum fitting with *Fermi*/GBM and HXMT data has been respectively performed for PRE, ME and EE. But since there is a significant saturation effect (data loss) during ME in HXMT, so in this emission only *Fermi*/GBM data has been used. The Bayesian Information Criterion (BIC) ⁴⁰ is used to measure the goodness of fit and determine the best model, we fitted with Band, Compton, Blackbody, Band + Blackbody and Compton + Blackbody models, since the Compton compared to the included blackbody models $\Delta BIC > 8$, the best model of the precursors is non-thermal spectrum Compton, which have ‘decisive’ evidence ⁴¹ against the models with higher criterion values. The time-averaged luminosity of the precursor of GRB 211211A is $2.6^{+0.1}_{-1.3} \times 10^{49}$ erg/s, the total energetics estimates to $7.7^{+0.4}_{-1.7} \times 10^{48}$ erg.

6 Search for periodic signals in the precursor

The regularly distributed spikes superimposed on the overall shape of the precursor suggest that there may exist Quasi-Periodical-Oscillations (QPO). In order to estimate the centroid frequency and significance of the possible QPOs, we have analysed the BAT and GBM lightcurves using several different methods.

The weighted wavelet Z-transform method and the Lomb-Scargle Periodogram method

We first employ one of the most widely used methods, the Weighted Wavelet Z-transform (WWZ) ¹⁶, to obtain the power spectra of GBM and BAT light-curves. Strong peaks at 22^{+3}_{-2} Hz (GBM) and 22^{+3}_{-1} Hz (BAT) (with period cycle of 45^{+5}_{-4} ms (GBM) and 45^{+5}_{-2} ms (BAT)) are found in the WWZ power spectra (Figure. 3), suggesting the existence of QPOs. The uncertainty of the QPO frequency is the full width at half maximum of the peak. And then, we also use another widely used method, the generalized Lomb-Scargle Periodogram (LSP) ^{18,44,45} to obtain the power spectra of GBM and BAT light-curves, which also show strong peaks at $21.93^{+2.82}_{-1.25}$ Hz (GBM) and $21.62^{+2.51}_{-0.63}$ Hz (BAT) (with period cycle of $45.6^{+2.8}_{-5.2}$ ms (GBM) and $41.5^{+4.8}_{-1.4}$ ms (BAT)) Extended Data Figure. 8. The consistence of the two results also shows the reliability of the analyses.

To estimate the confidence level of the above QPO signature found with WWZ, we simulate 2×10^4 artificial light-curves based on GBM and BAT data using the REDFIT method ¹⁷. The GBM simulation results show that the signal has 3.0σ confidence level, and the BAT simulation results show that the signal has 2.0σ confidence level at ~ 22 Hz. The joint significance of the GBM and BAT data is 4.0σ .

The fast Fourier transform method We perform Fast Fourier analysis on the GBM and BAT lightcurves, respectively. The Leahy normalized power of the lightcurves of GBM and BAT with FRED subtracted are shown in Figure. 3, where potential QPOs at about 22.5 Hz can be found.

In order to estimate the significance of the 22.5 Hz QPOs, we use Monte Carlo simulations, a widely used tool to evaluate the timing results on a transient event whose profile is known. Specifically, for this precursor, we adopt the FRED function to fit the GBM and BAT lightcurves, and then utilize the Markov Chain Monte Carlo simulations (MCMCs) implemented in Python package `emcee` to generate many sets of FRED parameters of posterior probabilities shown in Extended Data Figure. 11. With each set of parameters, a FRED profile between -0.1 s and 0.3 s can be generated and a simulated lightcurve can be produced by adding the Poisson photon counting noise. Each simulated lightcurve will give a periodogram, and thus one can get the distribution of the periodograms at different Fourier frequencies.

The probability-value of the QPOs can be obtained by comparing the Leahy power⁴² at 22.5 Hz of the observed light curve to those from the above simulations, which is 1.67×10^{-5} for GBM and 0.001 for BAT, corresponding to 4.1 and 3.0 σ , respectively.

The auto-correlation analyses We make auto-correlation analyses for the FRED-subtracted precursor lightcurves of GBM and BAT. There are basically three steps. First we use the precursor (T0-0.1:T0+0.3 s) and the background (T0-9.0:T0-0.5) before the precursor to calculate the cross-correlations and get the distribution of the correlation values, which follows well a Gaussian distribution with the mean $ACF_{\text{mean}} (\sim 0)$ and a standard deviation of ACF_{std} . We then make the auto-correlation of the precursor and take the ACF as the value of the highest peak among the first four peaks on the right side. Finally we get the significance of the QPO with $(ACF - ACF_{\text{mean}})/ACF_{\text{std}}$. The significance for GBM and BAT lightcurves are 4.3 σ and 3.3 σ (Extended Data Figure. 9), respectively; the joint significance is 5.8 σ , since the GBM data and BAT data are independent.

We further create two FRED-subtracted precursor lightcurves from the GBM data in energy bands 8-35 keV and 35-200 keV (with similar net counts in the two bands) to do the auto-correlation analysis separately. The QPO significance inferred with the above mentioned process are 3.3 σ and 3.0 σ , respectively, implying that the QPO signals are present in the whole energy band of 8-200 keV. Similarly, the QPO significance can be also inferred from the cross-correlation between the lightcurves in these two energy ranges, which is 4.0 σ . Besides, the high energy lightcurve leads the low energy one by 5_{-5}^{+7} ms, consistent with the spectral lag (11 ± 2 ms for 8-35 keV compared to 35-200 keV) in the total emission of the precursor. This may suggest that the QPO signal shares the same radiation process with the precursor itself.

The Z^2 method We also use the GBM data (detectors n0,n1,n2,n5,n9 and na, 8–200 keV) to search for periodic signal with Z-squared (Z^2 , the harmonic=1) around 25 Hz in the precursor

via *stingray*⁴³ and find QPOs of ~ 23.49 Hz with a significance of about 7.31σ (Extended Data Figure. 10). The same analyses applied to the BAT data reveal QPOs at 21.87 Hz with a significance of 3.86σ . Here the significance is obtained with simulations, i.e., we simulated a large number of lightcurves based on the FRED profile and calculate the Z^2 of each lightcurve, and the p-value of the QPOs is obtained by comparing the Z^2 of the real lightcurves to those of the simulated ones. We note here that the significance of the Z^2 method may be overestimated⁹⁶ due to the deviation from the standard χ^2 -distribution at each frequency.

7 Spectral Lag - L_{iso} correlation.

The Li-CCF^{60,61} is defined as

$$\text{MCCF}(k, \Delta t) = \frac{1}{M_{\Delta t}} \sum_{m=1}^{M_{\Delta t}} \sum_i u_m(i; \Delta t) v_{m+k}(i; \Delta t) / \sigma_u \sigma_v, \quad (3)$$

where $x(j; \delta t)$ and $y(j; \delta t)$ are the high time resolution initial lightcurves in two different energy bands, and combination starts from the m -th bin of the initial lightcurves, the phase factor $m = 1, 2, \dots, M_{\Delta t}$, and $u_m(\Delta t)$ and $v_m(\Delta t)$ are the background-subtracted series of $x_m(\Delta t)$ and $y_m(\Delta t)$ by re-binning the initial series,

$$\begin{aligned} u_m(i; \Delta t) &= x_m(i; \Delta t) - b_{x_m}(i; \Delta t), \\ v_m(i; \Delta t) &= y_m(i; \Delta t) - b_{y_m}(i; \Delta t), \\ \sigma_u^2 &= \sum_i u_m(i; \Delta t)^2, \\ \sigma_v^2 &= \sum_i v_m(i; \Delta t)^2, \end{aligned} \quad (4)$$

where b_{x_m} and b_{y_m} are the estimated background counts of lightcurves $x_m(\Delta t)$ and $y_m(\Delta t)$, respectively. We implement a Monte Carlo simulation of the observed lightcurves based on Gaussian (for BAT) or Poisson (for GBM) probability distribution to obtain the uncertainty of spectral lag.

Lag-peak luminosity correlation exists for pulses both within and across long GRBs with positive spectral lag^{54,55}. Therefore, the lag is an indicator of both GRB peak luminosity and time history morphology, with short-lag and variable bursts having greater luminosities than long-lag and smooth bursts⁵⁶⁻⁵⁹. Spectral lag of ME and EE of GRB 211211A in 200-250 keV compared to that in 100-150 keV at rest frame (corresponding to the observed energy of $[200-250]/(1+z)$ keV and $[100-150]/(1+z)$ keV, which is the same as in⁵⁸) are 3.6 ± 1.6 ms and 3.2 ± 6.9 ms, respectively, which are typical values of short bursts (see Figure. 2). Besides, the spectral lag of ME and EE are consistent within error, possibly indicating a similar origin. The spectral lag of the precursor is -7.4 ± 20.5 ms, which is due to the fact that the precursor signal is weak when energy > 200 keV and therefore the error is much larger.

We also obtain the SGRBs common intrinsic spectral lag is 0.001 ± 0.003 s (3σ), from the 46 SGRBs with redshift measurements observed by Swift/BAT or Fermi/GBM from November 2004 to December 2020⁶¹. We also calculate the spectral lag of GRB 170817A, the GRB of the binary neutron star merger, as 0.118 ± 0.140 s. The spectral lags of GRB 060614 and GRB 211227A, which are long duration burst but may be from compact star mergers^{62,63}, are 0.003 ± 0.006 s and -0.013 ± 0.024 (1σ), respectively. Figure. 2 shows that GRB 060614, GRB 170817A, GRB 211227A and GRB 211211A are out of the correlation of LGRBs.

8 Minimum Variability Timescale

The minimum timescale (Δt_{\min}) on which a GRB exhibits significant flux variations is believed to provide upper limit as to the size of the emitting region, the lower limit of the Lorentz factor and potentially shedding light on the nature of emission mechanism⁷⁵. The median minimum timescale in the rest frame (i.e. $\Delta t_{\min}/(1+z)$) for LGRBs and SGRBs of 45 and 10 ms, respectively⁷⁶. We employ the Bayesian Blocks algorithm and define the 1/2 shortest significant structures of blocks as the duration of minimum time interval⁷⁷. The minimum timescale of GRB 211211A is about 10 ms at 10-1000 keV, which is more consistent with SGRBs rather than LGRBs. We also adopt the continuous wavelet transform (CWT) method⁷⁷ and the results are consistent.

9 No accompanied Supernova and detection of a Kilonova.

The Ningbo Bureau of Education and Xinjiang Observatory Telescope (NEXT) located at Nanshan, Xinjiang, China started observations 9.85 hr after the GBM trigger. Over the next two weeks, NEXT carried out multi-band photometry in the Sloan r-, i- and z- filters. In the first night of the burst, the optical counterpart was clearly detected in our Sloan r-band stacked image, as shown in Extended Data Figure. 1. However, only upper limits were obtained in the following observations. We then turned to the 2.16 m telescope (short as XL216⁶⁴) located at Xinglong, Hebei, China, 26.35 days after the GBM trigger for images as deep as possible.

The data reduction was done by the standard process using the *IRAF* package⁶⁵. We performed aperture photometry at the burst position and calibrated with the Sloan Digital Sky Survey 14th data release⁶⁶. We also collected observational results at other telescopes that are public at Gamma-ray Coordinates Network (GCN). The whole photometric results are listed in Extended Data Table. 2.

We retrieved 10 keV X-ray data from the UK Swift Science Data Centre^{67,68}. The lightcurves in X-ray, optical and near-infrared are shown in Extended Data Figure. 2. A broken powerlaw⁶⁹ decay is used to fit the lightcurve. We only consider Sloan-r band for the optical as data in other optical bands are fewer. R and Rc data were converted to Sloan-r by simply adding 0.2 mag. The break time in optical and X-ray is $\log t_{O,b} = 5.19^{+0.07}_{-0.06}$ s and $\log t_{X,b} = 4.70^{+0.04}_{-0.04}$ s, respectively. The optical and X-ray decay index before and after their breaks are $\alpha_{O,1} = 1.29^{+0.07}_{-0.07}$, $\alpha_{O,2} = 2.98^{+0.79}_{-0.59}$, $\alpha_{X,1} = 1.06^{+0.05}_{-0.05}$, $\alpha_{X,2} = 3.03^{+0.26}_{-0.25}$, respectively. As can be seen,

the break time in optical is about 1 day later than in X-ray, and the post-break decay indices in optical and in X-ray are consistent with each other.

The observed r-band lightcurves of SN2010bh, SN2006aj, and SN1998bw at $z = 0.076$ (dashed dot lines) are shown in Extended Data Figure. 2. Our late optical upper limits rule out any GRB-associated broad-lined Type Ic supernova in GRB 211211A.

The *afterglowpy*⁷⁰ is used to fit the full X-ray data, the early optical data (i.e., earlier than ~ 0.3 day post-burst), and the early *Swift*/UVOT data⁷¹, because the late optical/near-infrared lightcurves have contribution from an excess component. We considered Top-Hat jet model and uniform interstellar medium (ISM) around the burst. The model contains seven free parameters, i.e., isotropic equivalent kinetic energy ($E_{K,iso}$), the circum-burst density (n), the half-opening angle of the jet (θ_c), the viewing angle (θ_{obs}), the electron distribution index (p), the fraction of electrons energy (ϵ_e) and the fraction of magnetic field energy (ϵ_B). We used *emcee* Python package to explore the parameter space to find the best-fit values of physical parameters⁷². The fitting afterglow (AG) lightcurves (dotted lines) are shown in Extended Data Figure. 2 and the fitting parameters listed in Extended Data Table. 3. The excess is similar to the prototype kilonova (KN), AT 2017gfo in GW 170817, at $z = 0.076$. The excess is fitted with a numerical two-component KN model developed by ourselves, which is similar to the KN model in *MOSTFIT*⁷³. The fitting AG + KN lightcurves (solid lines) are present for comparison with the fitting AG + AT 2107gfo lightcurves (dashed lines).

10 Magnetar flare model

For a typical magnetar, the strength of the surface dipolar magnetic field is $\sim 10^{14-15}$ Gauss. It means that the tension of the internal magnetic field (inside the magnetar) is strong enough to cause the observed ~ 22 Hz QPO; for example, the QPO frequency can be easily tuned to be consistent with the torsional mode $(l, n) = (2, 0)$ supported by the highly tangled internal magnetic field, as shown by Eq. (9) in²², with the model parameters set to be the same as known magnetars. According to the magnetic dipole model, the total energy of the magnetosphere outside the magnetar surface can be estimated as $E_{sph} \sim 2.0 \times 10^{46} - 2.0 \times 10^{48}$ erg. The magnetic energy inside the magnetar crust can be one or two orders of magnitudes higher than E_{sph} . So the total magnetic energy of the magnetar system is large enough to produce the observed precursor.

Considering its total duration, the precursor might be produced ~ 0.2 s before the coalescence. Using the quadrupole formula for GW emission, the time it takes for the binary companions to coalescence could be expressed as⁸¹

$$\tau_{GW} \approx 0.48 \text{ s} \left(\frac{P_b}{10 \text{ ms}} \right)^{8/3} \left(\frac{\mu}{M_\odot} \right)^{-1} \left(\frac{M_1 + M_2}{M_\odot} \right)^{-2/3} (1 - e^2)^{7/2}, \quad (5)$$

where M_1 and M_2 are NS masses, $\mu = M_1 M_2 / (M_1 + M_2)$ is the reduced mass, and e is the orbital eccentricity of the binary system. For a typical case with $M_1 = M_2 = 1.4 M_\odot$

and $e = 0$, when 0.2 s before merging, the orbital period is about 8 ms. The corresponding orbital distance could be estimated as ~ 80 km with Kepler's law. At this distance, the tidal deformation of NSs is still weak, which could hardly affect the magnetar's torsional or crustal oscillations.

11 Pre-merger magnetosphere interaction model

The pre-merger magnetosphere interaction model can yield a nonthermal precursor^{35,36,38}, and the luminosity of the precursor from two NSs can be estimated as³¹

$$L_{\text{MI}} \approx 2.0 \times 10^{46} \eta B_{*,13}^2 (a/30 \text{ km})^{-7} \text{ erg s}^{-1}, \quad (6)$$

where $B_* = 10^{13} B_{*,13}$ G is the magnetic field of the main NS, a is the separation between the two NSs, and the efficiency parameter $0.01 \lesssim \eta \lesssim 1$ depends on the magnetic field structure of the binary system. The luminosity of the precursor of GRB 211211A is $2.5 \times 10^{49} \text{ erg s}^{-1}$, if we assume that the distance a is 30 km before disruption, the magnetic field of the main NS should be about $3.5 \times 10^{14} - 3.5 \times 10^{15} \text{ G}$, which is consistent with most known magnetars³⁹. However, it is worth to note that when $a = 30$ km, the orbital period is in order of millisecond, so it is difficult to produce a precursor lasting for 0.2 s. If the precursor is produced ~ 0.2 s before the coalescence, the main NS will need an extremely high magnetic field ($\sim 10^{16-17} \text{ G}$). It is interesting to note that within the context of such a model, the non-detection of precursors associated with GRB 170817A suggests an upper limit of magnetic field of $8 \times 10^{13} \text{ G}$ ³⁷.

29. Bromberg, O., Nakar, E., Piran, T. et al. Short versus long and collapsars versus non-collapsars: a quantitative classification of gamma-ray bursts. The Astrophysical Journal **764**, 179 (2013).
30. Xiao, S. et al. Deadtime calculation method of the high energy x-ray telescope (he) onboard the insight-hxmt satellite. Journal of High Energy Astrophysics **26**, 58–64 (2020).
31. Wang, J.-S., Peng, Z.-K., Zou, J.-H., Zhang, B.-B. & Zhang, B. Stringent search for precursor emission in short grbs from fermi/gbm data and physical implications. The Astrophysical Journal Letters **902**, L42 (2020).
32. Hu, Y.-D. et al. Internal energy dissipation of gamma-ray bursts observed with swift: precursors, prompt gamma-rays, extended emission, and late x-ray flares. The Astrophysical Journal **789**, 145 (2014).
33. Zhong, S.-Q., Dai, Z.-G., Cheng, J.-G., Lan, L. & Zhang, H.-M. Precursors in short gamma-ray bursts as a possible probe of progenitors. The Astrophysical Journal **884**, 25 (2019).
34. Norris, J. et al. Attributes of pulses in long bright gamma-ray bursts. The Astrophysical Journal **459**, 393 (1996).

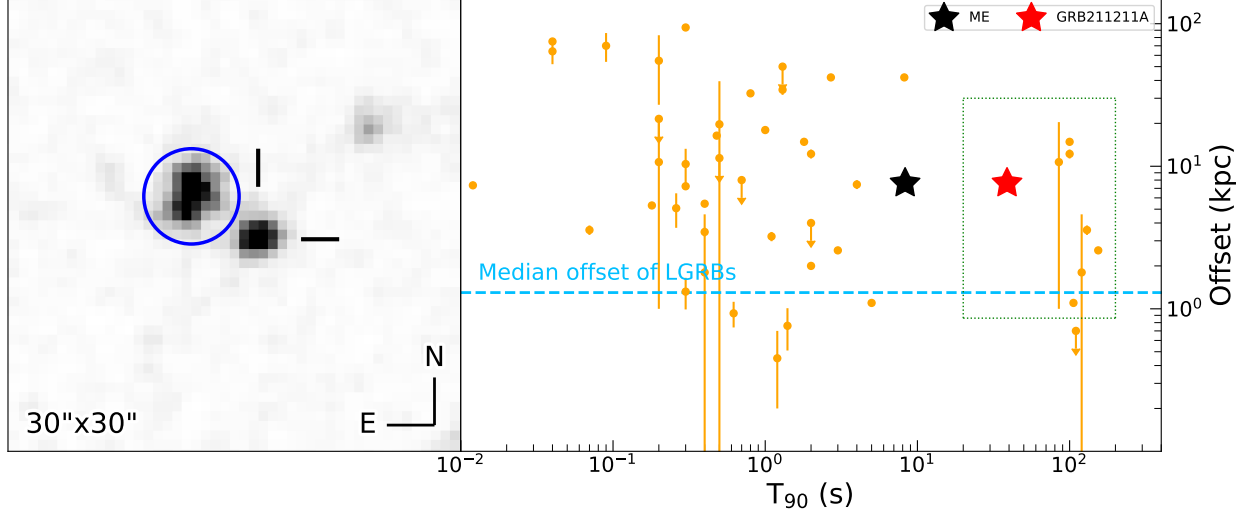
35. Lai, D. Dc circuit powered by orbital motion: magnetic interactions in compact object binaries and exoplanetary systems. The Astrophysical Journal Letters **757**, L3 (2012).
36. Palenzuela, C. et al. Electromagnetic and gravitational outputs from binary-neutron-star coalescence. Physical review letters **111**, 061105 (2013).
37. Abbott, B. P. et al. Gravitational waves and gamma-rays from a binary neutron star merger: Gw170817 and grb 170817a. The Astrophysical Journal Letters **848**, L13 (2017).
38. Wang, J.-S., Peng, F.-K., Wu, K. & Dai, Z.-G. Pre-merger electromagnetic counterparts of binary compact stars. The Astrophysical Journal **868**, 19 (2018).
39. Olausen, S. & Kaspi, V. The mcgill magnetar catalog. The Astrophysical Journal Supplement Series **212**, 6 (2014).
40. Schwarz, G. Estimating the dimension of a model. The annals of statistics 461–464 (1978).
41. Liddle, A. R. Information criteria for astrophysical model selection. Monthly Notices of the Royal Astronomical Society: Letters **377**, L74–L78 (2007).
42. Van der Klis, M. Fourier techniques in x-ray timing. In Timing neutron stars, 27–69 (Springer, 1989).
43. Bachetti, M. et al. Stingraysoftware/stingray: Version 1.0 (2022). URL <https://doi.org/10.5281/zenodo.6394742>.
44. Lomb, N. R. Least-squares frequency analysis of unequally spaced data. Astrophysics & Space Science **39**, 447–462 (1976).
45. Scargle, J. & D. Studies in astronomical time series analysis. ii - statistical aspects of spectral analysis of unevenly spaced data. ApJ **263**, 835–835 (1982).
46. Tsvetkova, A. et al. The konus-wind catalog of gamma-ray bursts with known redshifts. i. bursts detected in the triggered mode. The Astrophysical Journal **850**, 161 (2017).
47. von Kienlin, A. et al. The fourth fermi-gbm gamma-ray burst catalog: a decade of data. The Astrophysical Journal **893**, 46 (2020).
48. Amati, L. et al. Measuring the cosmological parameters with the e p, i–e iso correlation of gamma-ray bursts. Monthly Notices of the Royal Astronomical Society **391**, 577–584 (2008).
49. Zhang, B. et al. Discerning the physical origins of cosmological gamma-ray bursts based on multiple observational criteria: the cases of $z=6.7$ grb 080913, $z=8.2$ grb 090423, and some short/hard grbs. The Astrophysical Journal **703**, 1696 (2009).
50. Nava, L. et al. A complete sample of bright swift long gamma-ray bursts: testing the spectral-energy correlations. Monthly Notices of the Royal Astronomical Society **421**, 1256–1264 (2012).

51. Zou, Y.-C. et al. newblock Determining the lorentz factor and viewing angle of grb 170817a. The Astrophysical Journal Letters **852**, L1 (2017).
52. Minaev, P. Y. & Pozanenko, A. newblock The e p, i–e iso correlation: type i gamma-ray bursts and the new classification method. Monthly Notices of the Royal Astronomical Society **492**, 1919–1936 (2020).
53. Pozanenko, A. et al. Grb 170817a associated with gw170817: multi-frequency observations and modeling of prompt gamma-ray emission. The Astrophysical Journal Letters **852**, L30 (2018).
54. Norris, J. P., Marani, G. F. & Bonnell, J. T. Connection between energy-dependent lags and peak luminosity in gamma-ray bursts. The Astrophysical Journal **534**, 248 (2000).
55. Hakkila, J., Giblin, T. W., Norris, J. P., Fragile, P. C. & Bonnell, J. T. Correlations between lag, luminosity, and duration in gamma-ray burst pulses. The Astrophysical Journal Letters **677**, L81 (2008).
56. Norris, J. P. Implications of the lag-luminosity relationship for unified gamma-ray burst paradigms. The Astrophysical Journal **579**, 386 (2002).
57. Hakkila, J. et al. A gamma-ray burst database of batse spectral lag and internal luminosity function values. The Astrophysical Journal Supplement Series **169**, 62 (2007).
58. Ukwatta, T. et al. The lag–luminosity relation in the grb source frame: an investigation with swift bat bursts. Monthly Notices of the Royal Astronomical Society **419**, 614–623 (2012).
59. Shao, L. et al. A new measurement of the spectral lag of gamma-ray bursts and its implications for spectral evolution behaviors. The Astrophysical Journal **844**, 126 (2017).
60. Li, T.-P. et al. Timescale analysis of spectral lags. Chinese Journal of Astronomy and Astrophysics **4**, 583 (2004).
61. Xiao, S. et al. A robust estimation of lorentz invariance violation and intrinsic spectral lag of short gamma-ray bursts. The Astrophysical Journal Letters **924**, L29 (2022).
62. Gehrels, N. et al. A new γ -ray burst classification scheme from grb 060614. Nature **444**, 1044–1046 (2006).
63. Lü, H.-J. et al. Grb 211227a as a peculiar long gamma-ray burst from compact star merger. arXiv preprint arXiv:2201.06395 (2022).
64. Fan, Z. et al. The Xinglong 2.16-m Telescope: Current Instruments and Scientific Projects. Publications of the Astronomical Society of the Pacific **128**, 115005 (2016).
65. Tody, D. The IRAF Data Reduction and Analysis System. In Crawford, D. L. (ed.) Instrumentation in astronomy VI, vol. 627 of Society of Photo-Optical Instrumentation Engineers (SPIE) Conference Series, 733 (1986).

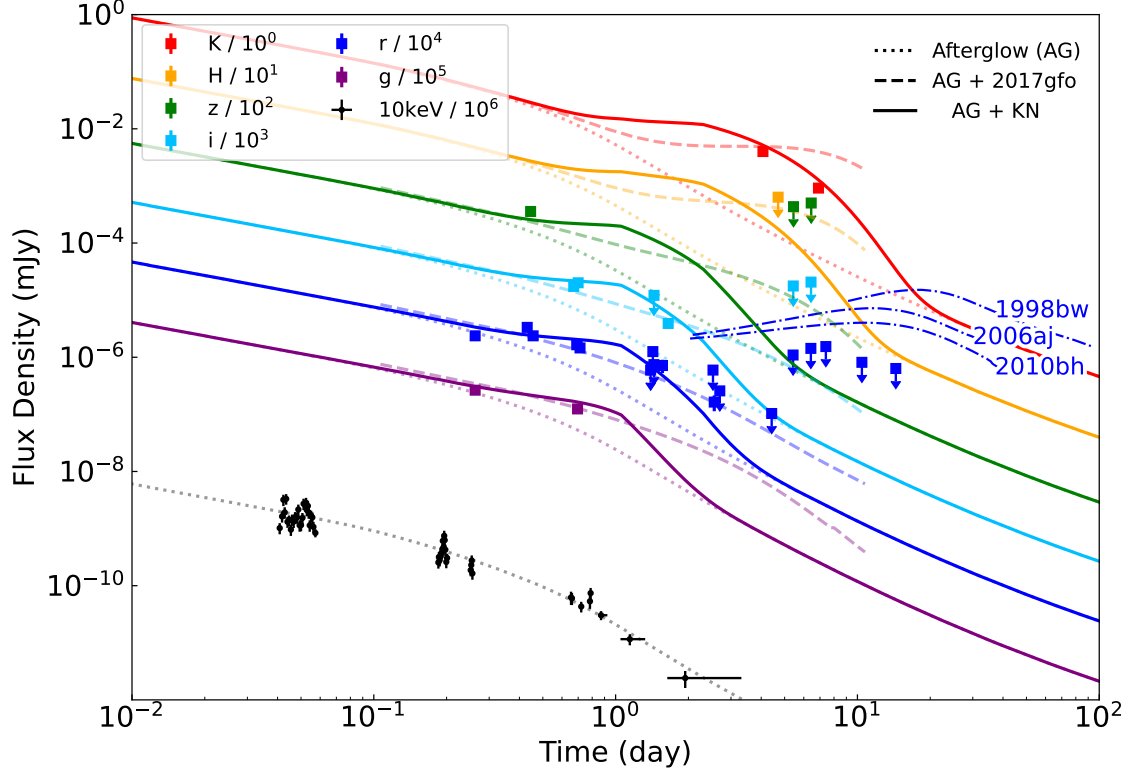
66. Abolfathi, B. et al. The Fourteenth Data Release of the Sloan Digital Sky Survey: First Spectroscopic Data from the Extended Baryon Oscillation Spectroscopic Survey and from the Second Phase of the Apache Point Observatory Galactic Evolution Experiment. The Astrophysical Journal Supplement Series **235**, 42 (2018).
67. Evans, P. A. et al. An online repository of Swift/XRT lightcurves of γ -ray bursts. Astronomy & Astrophysics **469**, 379–385 (2007).
68. Evans, P. A. et al. Methods and results of an automatic analysis of a complete sample of Swift-XRT observations of GRBs. Monthly Notices of the Royal Astronomical Society **397**, 1177–1201 (2009).
69. Beuermann, K. et al. VLT observations of GRB 990510 and its environment. arXiv preprint astro-ph/9909043 **352**, L26–L30 (1999).
70. Ryan, G., van Eerten, H., Piro, L. & Troja, E. Gamma-Ray Burst Afterglows in the Multimessenger Era: Numerical Models and Closure Relations. The Astrophysical Journal **896**, 166 (2020).
71. Belles, A. et al. GRB 211211A: Swift/UVOT detection. GRB Coordinates Network **31222**, 1 (2021).
72. Foreman-Mackey, D., Hogg, D. W., Lang, D. & Goodman, J. emcee: The MCMC Hammer. Publications of the Astronomical Society of the Pacific **125**, 306 (2013).
73. Guillochon, J. et al. MOSFiT: Modular Open Source Fitter for Transients. The Astrophysical Journal Supplement Series **236**, 6 (2018).
74. Goldstein, A. et al. An ordinary short gamma-ray burst with extraordinary implications: Fermi-gbm detection of grb 170817a. The Astrophysical Journal Letters **848**, L14 (2017).
75. SCHMIDT, W. K. Distance limit for a class of model γ -ray burst sources. Nature **271**, 525–527 (1978).
76. Golkhou, V. Z., Butler, N. R. & Littlejohns, O. M. The energy dependence of grb minimum variability timescales. The Astrophysical Journal **811**, 93 (2015).
77. Vianello, G. et al. The bright and the slow—grbs 100724b and 160509a with high-energy cutoffs at $\lesssim 100$ mev. The Astrophysical Journal **864**, 163 (2018).
78. Troja, E., King, A. R., O’Brien, P. T., Lyons, N. & Cusumano, G. Different progenitors of short hard gamma-ray bursts. Monthly Notices of the Royal Astronomical Society: Letters **385**, L10–L14 (2008).
79. Berger, E. Short-Duration Gamma-Ray Bursts. Annual review of Astronomy and Astrophysics **52**, 43–105 (2014).

80. Fong, W. et al. Demographics of the Galaxies Hosting Short-duration Gamma-Ray Bursts. The Astrophysical Journal **769**, 56 (2013).
81. Peters, P. C. Gravitational radiation and the motion of two point masses. Physical Review **136**, B1224 (1964).
82. Ito, N. et al. GRB 211211A: MITSuME Akeno optical observation. GRB Coordinates Network **31217**, 1 (2021).
83. Kumar, H. et al. GRB 211211A: HCT and GIT optical follow up observations. GRB Coordinates Network **31227**, 1 (2021).
84. de Ugarte Postigo, A. et al. GRB 211211A: Afterglow detection from CAFOS/2.2m CAHA. GRB Coordinates Network **31218**, 1 (2021).
85. Malesani, D. B. et al. GRB 211211A: NOT optical spectroscopy. GRB Coordinates Network **31221**, 1 (2021).
86. Strausbaugh, R. & Cucchiara, A. GRB 211211A: LCO Optical Observations. GRB Coordinates Network **31214**, 1 (2021).
87. Mao, J., Xin, Y. X. & Bai, J. M. GRB 211211A: GMG upper limit. GRB Coordinates Network **31232**, 1 (2021).
88. Gupta, R. et al. GRB 211211A: observations with the 3.6m Devasthal Optical Telescope. GRB Coordinates Network **31299**, 1 (2021).
89. Pankov, N. et al. GRB 211211A: AbAO optical observations. GRB Coordinates Network **31233**, 1 (2021).
90. de Ugarte Postigo, A. et al. GRB 211211A: Further observations from CAFOS/2.2m CAHA. GRB Coordinates Network **31228**, 1 (2021).
91. Moskvitin, A. et al. GRB 211211A: SAO RAS optical observations. GRB Coordinates Network **31234**, 1 (2021).
92. Levan, A. J. et al. GRB 211211A - Gemini K-band detection. GRB Coordinates Network **31235**, 1 (2021).
93. D'Avanzo, P. et al. GRB 211211A: TNG NIR observations. GRB Coordinates Network **31242**, 1 (2021).
94. Rastinejad, J. et al. GRB 211211A: MMT/MMIRS Observations Indicate Fading of K-band Source. GRB Coordinates Network **31264**, 1 (2021).
95. Schlafly, E. F. & Finkbeiner, D. P. Measuring Reddening with Sloan Digital Sky Survey Stellar Spectra and Recalibrating SFD. The Astrophysical Journal **737**, 103 (2011).

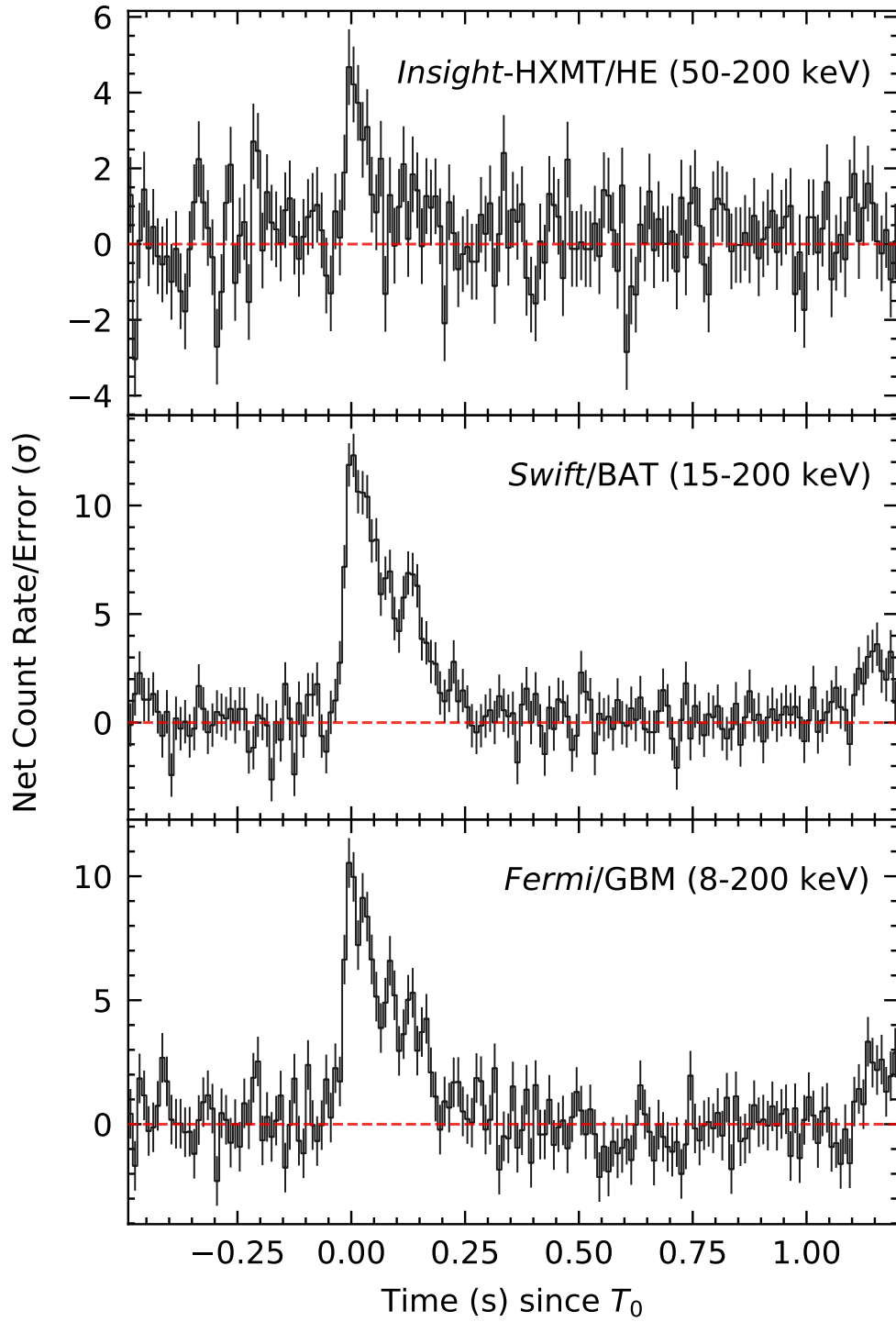
96. Hübner, M., Huppenkothen, D., Lasky, P. D. & Inglis, A. R. Pitfalls of periodograms: The nonstationarity bias in the analysis of quasiperiodic oscillations. *The Astrophysical Journal Supplement Series* **259**, 32 (2022).



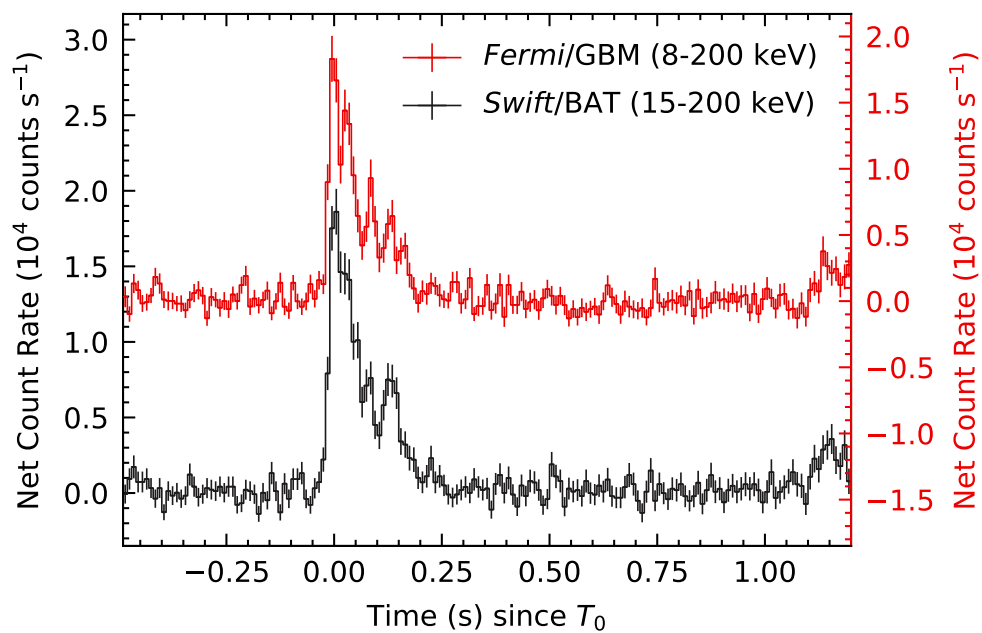
Extended Data Figure. 1: **Left Panel:** The field view of GRB 211211A, which is at the center of the Nanshan/NEXT Sloan-r band image, obtained 0.43 day after the burst trigger. The nearby galaxy circled in blue has a spectroscopic redshift of $z = 0.076$ ⁶. The offset between the burst and the nucleus of the galaxy is 5.11 ± 0.23 arcsec, which leads to a chance coincidence probability of $\sim 1.1\%$ between the burst and the galaxy⁷. The small probability confirms the galaxy as the host of the burst. **Right Panel:** The duration (T_{90}) v.s. offsets for Short GRBs (SGRBs; Type I) and Long GRBs (LGRBs; Type II). The collected SGRB points^{78–80} are shown in orange dots. SGRBs with extended emissions (EEs) are circled by a green dotted rectangle. The blue dashed line is the median offset for LGRBs⁷. The main emission (ME) and the total emission of GRB 211211A are marked with a black star and a red star, respectively.



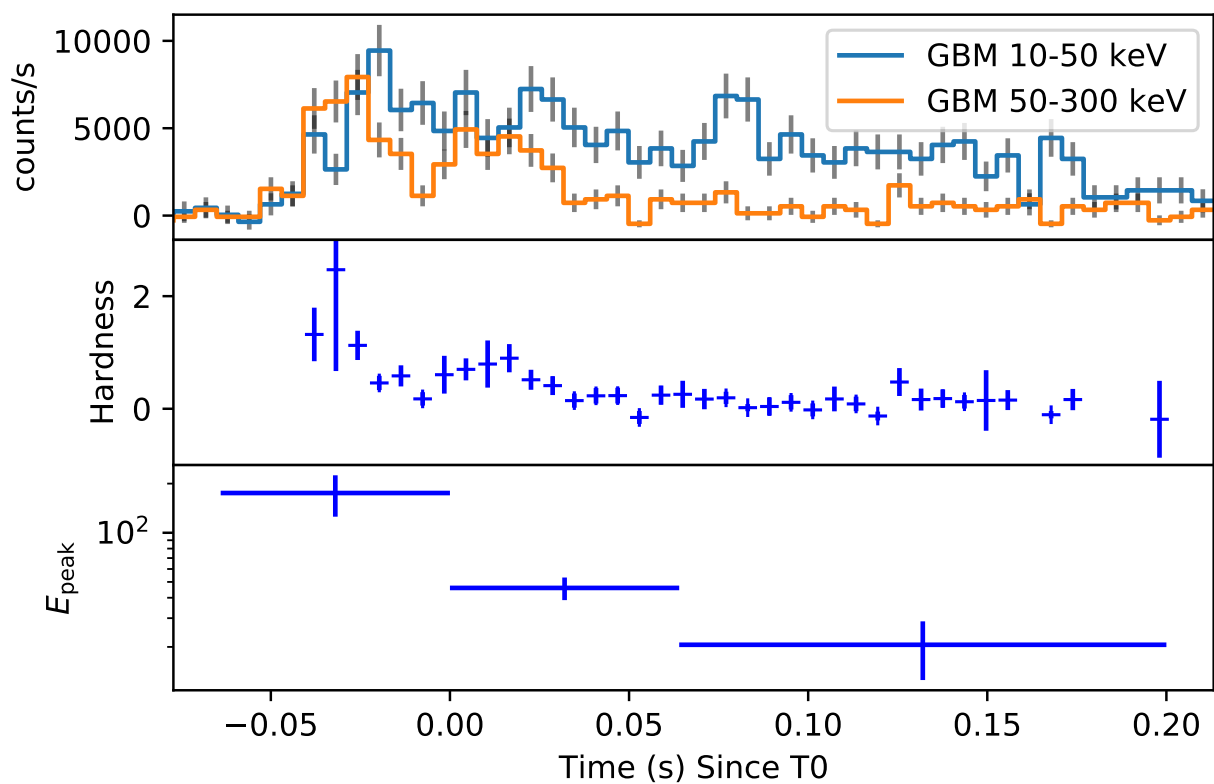
Extended Data Figure. 2: Follow-ups of GRB 211211A. For comparison, the observed r-band lightcurves of SN2010bh, SN2006aj, and SN1998bw at $z = 0.076$ are presented (dash dotted lines). Late optical upper limits rule out any GRB-associated broad-lined Type Ic supernova in GRB 211211A. The full X-ray data and early optical data are jointly fitted with the standard forward shock afterglow (AG) model (dotted lines). An excess in optical/near-infrared is evident after the AG subtraction, which is similar to the prototype kilonova (KN), AT 2017gfo in GW 170817, also placed at $z = 0.076$. The excess is fitted with a numerical two-component KN model developed in this work. The fitting AG + KN lightcurves (solid lines) are present for comparison with the fitting AG + AT 2107gfo lightcurves (dashed lines).



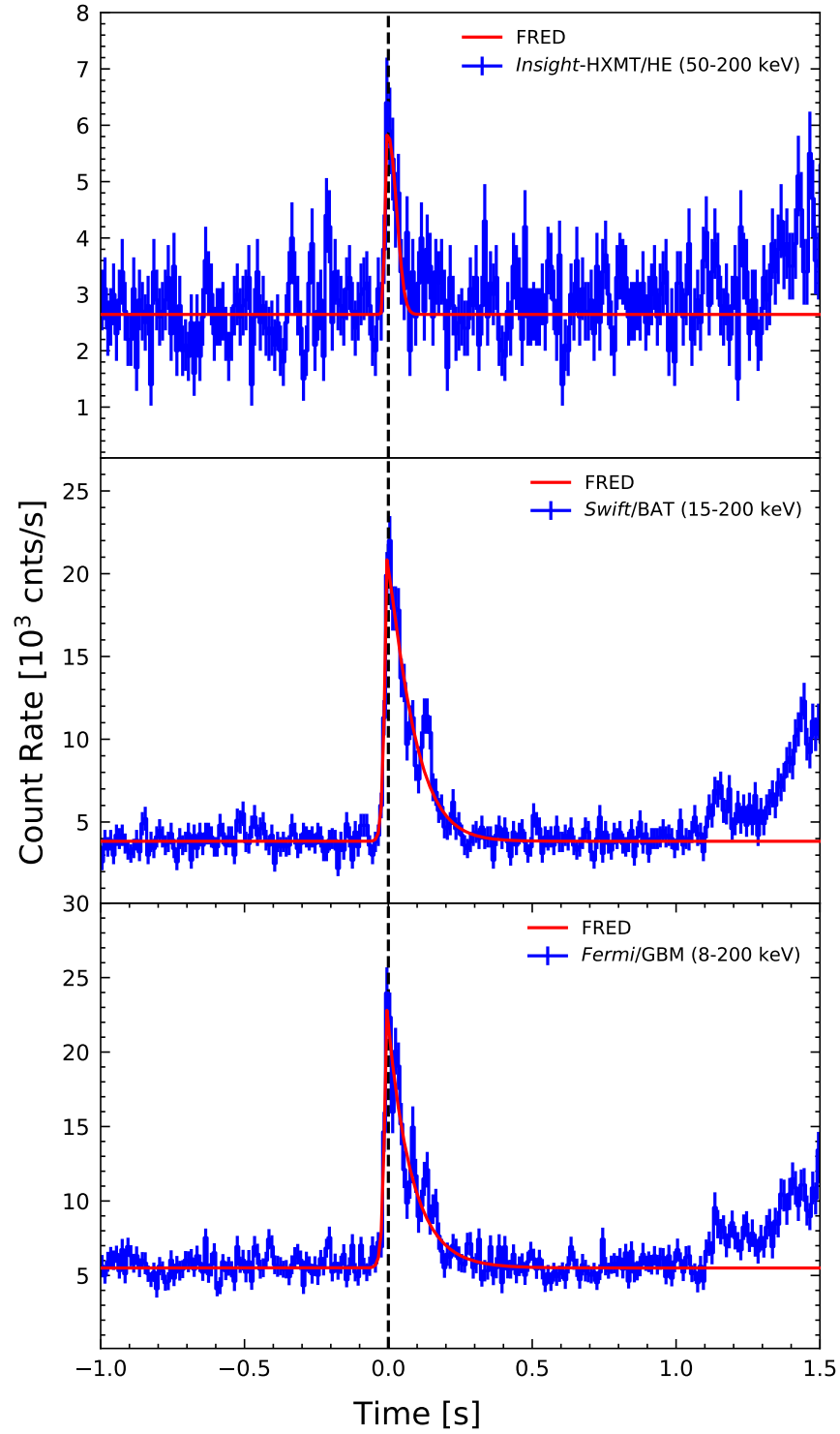
Extended Data Figure. 3: The weighted net lightcurves of three instruments, these curves are weighted by their errors accordingly. The curves indicate the counting excess level of the three instruments relative to the background, in unit of σ .



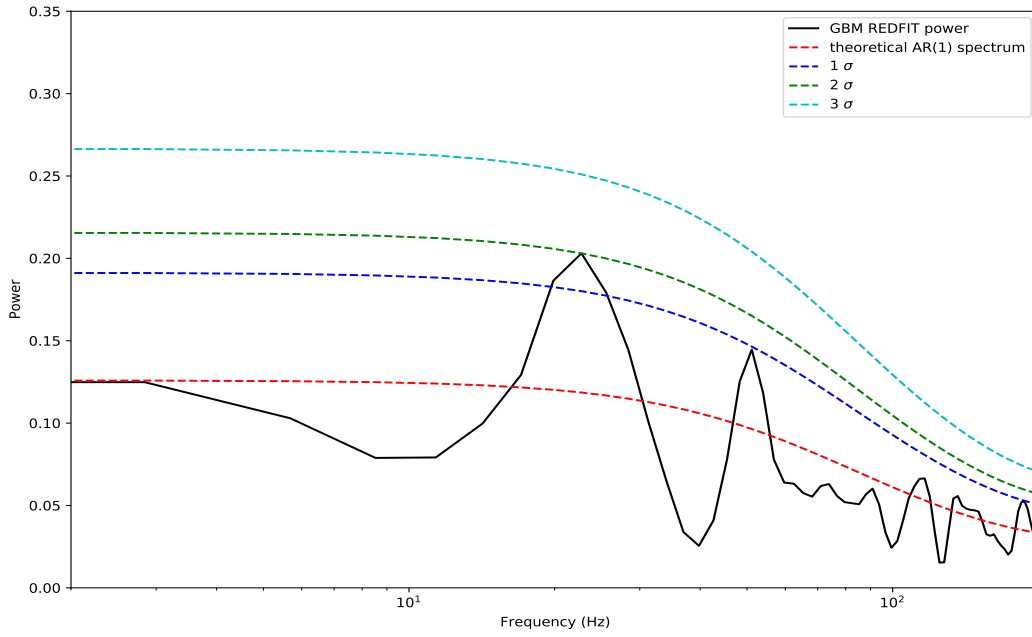
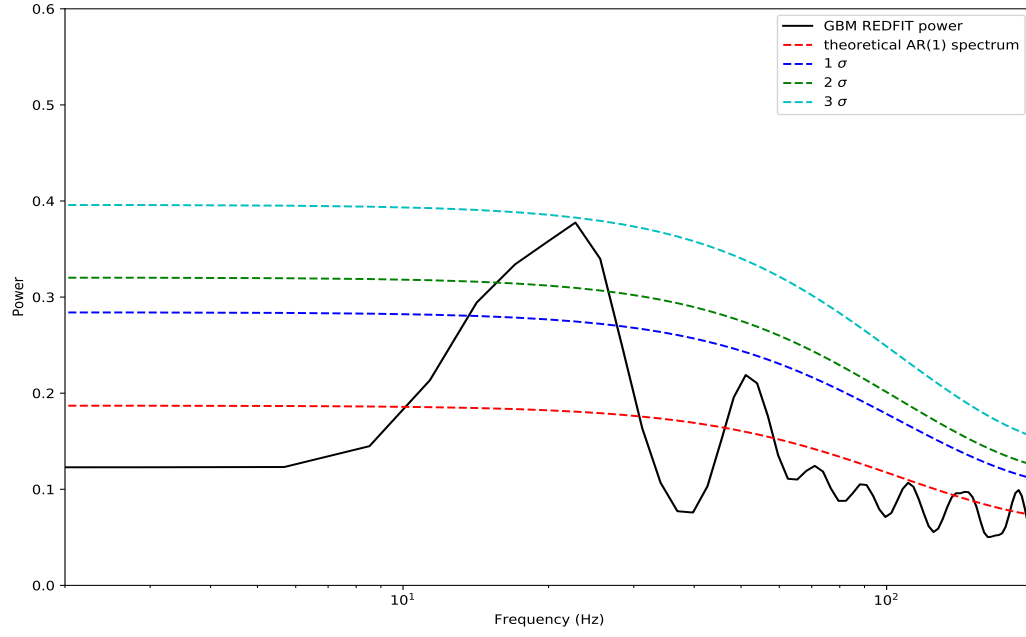
Extended Data Figure. 4: The net lightcurves of *Fermi*/GBM and *Swift*/BAT. These two curves are found to consist of some (quasi-)periodic pulses near T_0 .



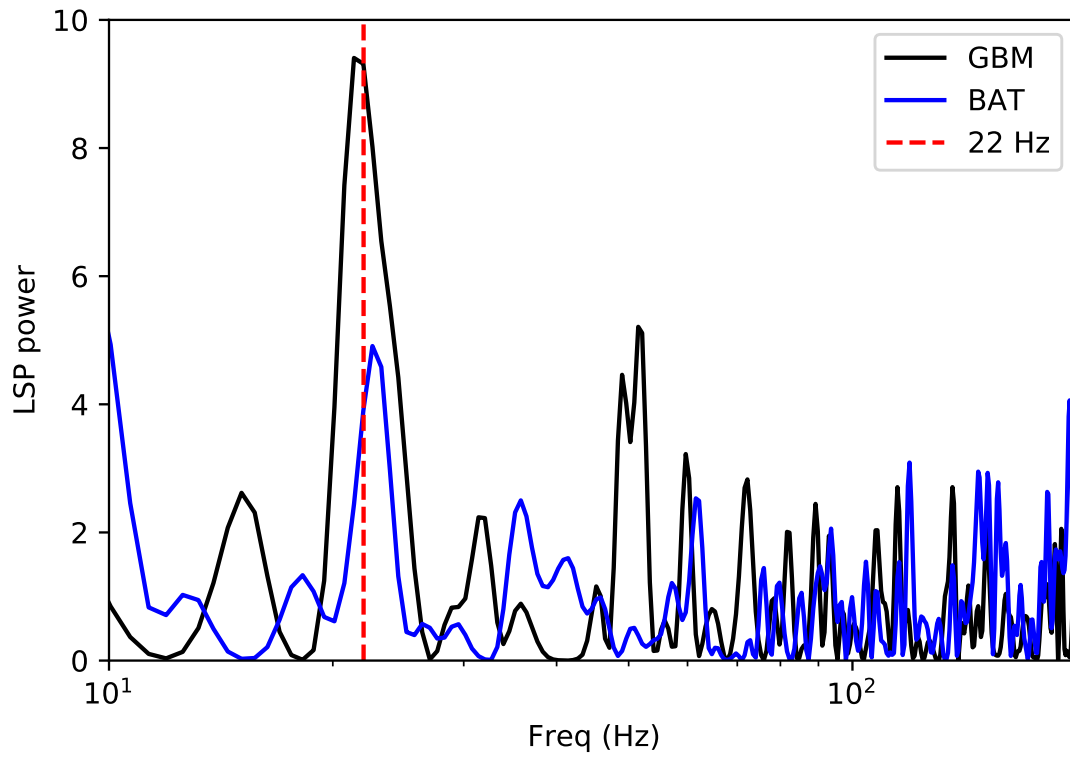
Extended Data Figure. 5: Hardness and E_{peak} evolution of the precursor.



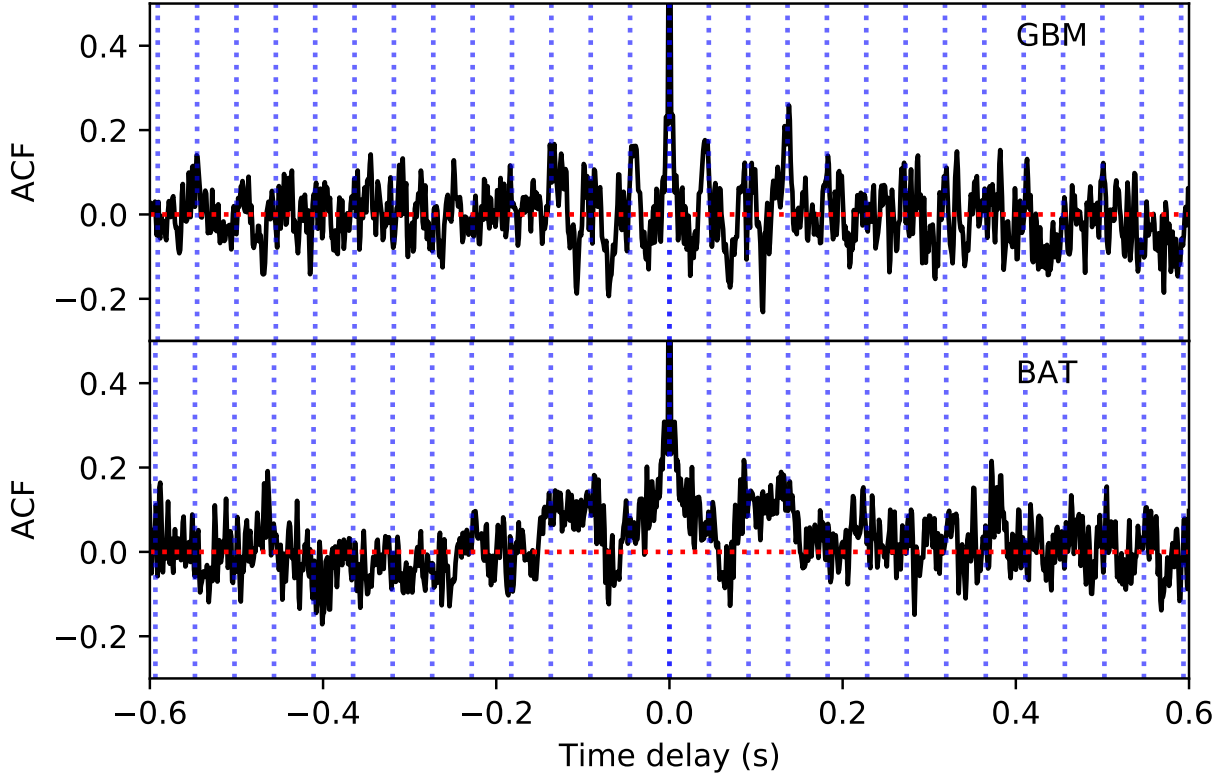
Extended Data Figure. 6: Observational lightcurves in blue lines detected by *Insight-HXMT/HE*, *Swift/BAT* and *Fermi/GBM* with the best-fitting lines modelled by the FRED functions in red respectively. The time bin size is 10 ms.



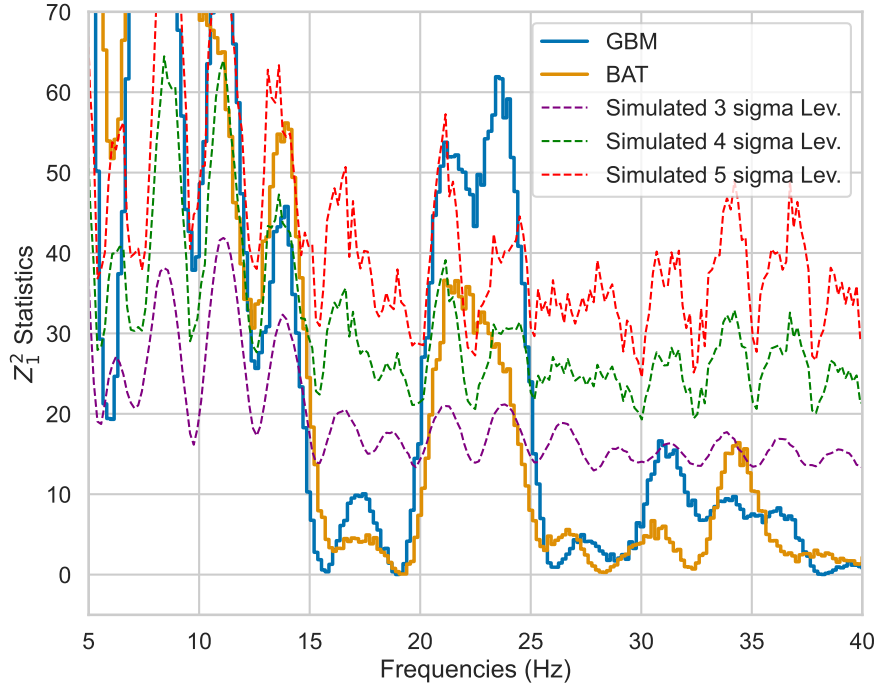
Extended Data Figure. 7: The redfit spectrum power of GBM and BAT in 8-200 keV at -0.1 s to 0.3 s. The red dash line represent the theoretical AR(1) spectrum, and the blue, green and cyan dash line represent 1σ , 2σ and 3σ false-alarm level, respectively.



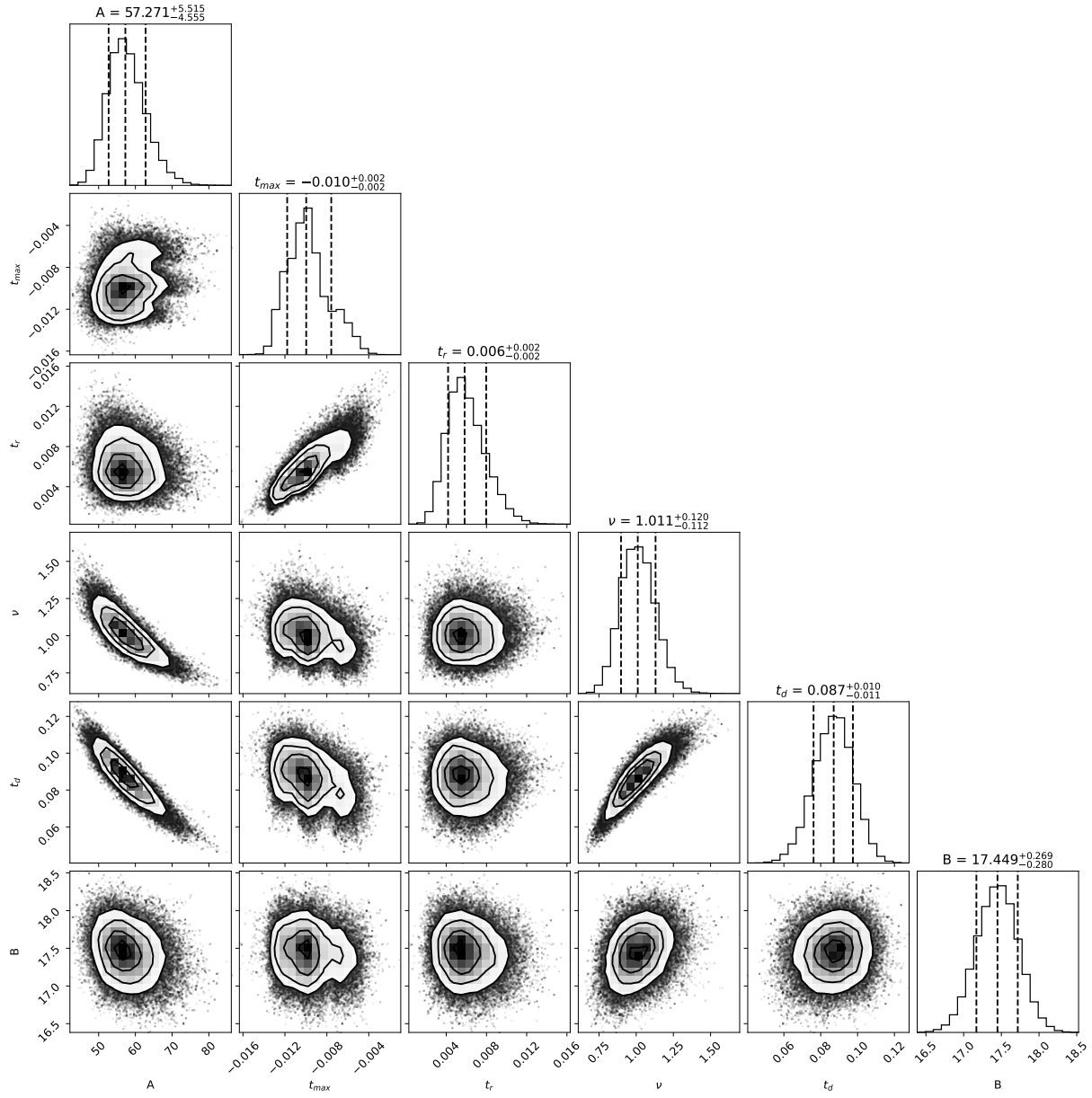
Extended Data Figure. 8: LSP power of GRB 211211A in 8-200 keV at -0.1 s to 0.3 s. The black and blue solid line represent LSP power of GBM and BAT, respectively. The red dash line (22 Hz) represent QPO frequency obtained from WWZ.



Extended Data Figure. 9: The ACF for GBM and BAT FRED-subtracted precursor lightcurves, respectively. The significant for GBM and BAT are 4.3σ and 3.3σ , respectively; the joint significance is 5.8σ , since the data of GBM and BAT are independent.



Extended Data Figure. 10: Periodogram of precursor for GBM and BAT observations. The purple, green, and black dashed lines represent 3, 4, and 5 σ significance at each frequency, respectively. The significance for GBM data at 23.49 Hz is 7.31σ and the BAT have a 3.86σ at 21.14 Hz. The significance are determined by the simulated distribution by drawing the photons from the FRED lightcurve obtained by fitting the precursor lightcurves. The joint significance is 8.5σ , since the data of GBM and BAT are independent.



Extended Data Figure. 11: The posterior distributions of parameters in the FRED model as described in eq.2 are presented on the diagonal. The off-diagonal panels show correlations between parameters. The scatter plots are selected from the last 4000 picked parameter pairs from the entire sample of 20000 parameter sets with 30 walkers.

Extended Data Table. 1: Spectral fitting with *Fermi*/GBM and *Insight*-HXMT/HE for GRB 211211A

Episode	Model	$E_{\text{cut},1}^*$ (keV)	α_1	β	$E_{\text{cut},2}^a$ (keV)	α_2	E_{iso} (erg)	E_{γ}^b (erg)	pgstat/dof
Precursor	Comp	-	-	-	83 ± 19	-1.12 ± 0.15	$7.72_{-1.71}^{+0.41} \times 10^{48}$	-	690/341
Main emission	Band+Comp	98 ± 14	-0.43 ± 0.13	-2.05 ± 0.02	1370 ± 57	-1.01 ± 0.04	$5.25_{-0.64}^{+0.01} \times 10^{51}$	6.56×10^{48}	872/447
Extended emission	Band+Comp	31 ± 7	-0.34 ± 0.28	-2.16 ± 0.04	438 ± 70	-1.26 ± 0.13	$2.23_{-0.52}^{+0.02} \times 10^{51}$	2.79×10^{48}	839/807
Full burst	Band+Comp	45 ± 8	-0.27 ± 0.20	-1.92 ± 0.02	1228 ± 65	-1.21 ± 0.04	$7.53_{-0.27}^{+0.01} \times 10^{51}$	-	1096/388

^a $E_{\text{cut}} = E_{\text{peak}}/(2+\alpha)$. The subscripts 1, 2 represent the parameters of Band and Compton, respectively.

^b Corrected for beaming effect with jet half-opening angle of 0.05 rad.

^c HXMT data only be used for spectrum fitting in Precursor and Extended emission.

Extended Data Table. 2: The photometric results of our observations. ΔT is the expose medium time after the GBM trigger. Magnitudes are corrected for Galactic Extinction, which is $E(B-V) = 0.02$ (⁹⁵).

$\Delta T(\text{days})$	Telescope/Observatory	Filter	Mag(AB)	Ref.
0.263	MITSuME	g	20.33 ± 0.20	(2)
0.263	MITSuME	Rc	20.25 ± 0.10	(2)
0.263	MITSuME	Ic	20.37 ± 0.30	(2)
0.431	NEXT	r	20.08 ± 0.06	(1)
0.445	NEXT	z	20.01 ± 0.23	(1)
0.456	HCT	R	20.25 ± 0.13	(3)
0.671	CAHA	i	20.79 ± 0.05	(4)
0.692	NOT	r	20.84 ± 0.05	(5)
0.700	LCO	R	20.99 ± 0.09	(6)
0.725	LCO	I	21.91 ± 0.25	(6)
1.396	GMG	r	>21.95	(7)
1.410	DOT	R	21.82 ± 0.07	(8)
1.425	GIT	r	>21.14	(3)
1.440	NEXT	r	>22.01	(1)
1.441	NEXT	i	>21.18	(1)
1.562	AS-32/AbAO	R	21.55 ± 0.33	(9)
1.650	CAHA	i	22.41 ± 0.09	(10)
2.527	AS-32/AbAO	R	>21.75	(9)
2.558	Zeiss-1000	Rc	>23.05	(11)
4.067	Gemini	K	22.39 ± 0.10	(12)
4.420	DOT	R	>23.86	(8)
4.700	TNG	H	>21.89	(13)
5.419	NEXT	r	>21.29	(1)
5.428	NEXT	i	>20.77	(1)
5.440	NEXT	z	>19.8	(1)
6.419	NEXT	r	>21.0	(1)
6.428	NEXT	i	>20.6	(1)
6.440	NEXT	z	>19.64	(1)
6.900	MMT	K	23.99	(14)
7.403	NEXT	r	>20.92	(1)
10.434	NEXT	r	>21.61	(1)
14.412	NEXT	r	>21.88	(1)
26.372	XL216	R	>23.21	(1)

References: (1) This work, (2) ⁸², (3) ⁸³, (4) ⁸⁴, (5) ⁸⁵, (6) ⁸⁶, (7) ⁸⁷, (8) ⁸⁸, (9) ⁸⁹, (10) ⁹⁰, (11) ⁹¹, (12) ⁹², (13) ⁹³, (14) ⁹⁴

Extended Data Table. 3: The afterglow fitting parameters.

Parameter	Value
$\log_{10}(E_{K,iso})/\text{erg}$	$52.66^{+1.13}_{-0.92}$
$\log_{10}(n)/\text{cm}^{-3}$	$0.03^{+1.27}_{-1.59}$
p	$2.05^{+0.03}_{-0.03}$
θ_c/rad	$0.05^{+0.03}_{-0.02}$
$\theta_{\text{obs}}/\text{rad}$	$0.03^{+0.03}_{-0.02}$
$\log_{10}(\epsilon_e)$	$-1.15^{+0.80}_{-1.28}$
$\log_{10}(\epsilon_B)$	$-4.58^{+1.23}_{-0.94}$

Extended Data Table. 4: Identification of precursor

Instrument	T_{pre} (s)	T_{wt} (s)	b_0^a (counts/s)	b_1^a (counts/s ²)	$\chi^2/\text{d.o.f}$	p-value	A^2/n	significance
<i>Insight</i> -HXMT/HE	0.08 (0.00:0.08)	1.28 (0.08:1.35)	2610.40 \pm 135.23	61.45 \pm 101.37	74.69/86	0.80	0.30/88	> 15 σ
<i>Swift</i> /BAT	0.22 (0.00:0.22)	0.88 (0.22:1.10)	3985.38 \pm 165.82	17.21 \pm 135.69	73.48/86	0.83	0.27/88	> 15 σ
<i>Fermi</i> /GBM	0.19 (-0.01:0.17)	0.93 (0.17:1.10)	5651.43 \pm 174.77	62.74 \pm 136.93	90.18/86	0.36	0.31/88	> 15 σ

^a b_0 is the background rate at T_0 , and b_1 is the background change rate.

Extended Data Table. 5: Time resolved spectral fitting of the precursor with *Fermi*/GBM, *Swift*/BAT and *Insight*-HXMT/HE for GRB 211211A

T_{Start}	T_{Stop}	Model	E_{peak} (keV)	Index	pgstat/dof	Exposure Time(s)	E_{iso} (erg)	L_{iso} (erg/s)
-0.064	0.000	Comp	176 \pm 50	0.77 \pm 0.20	3294.82/517	0.063	$2.7^{+0.7}_{-0.5} \times 10^{48}$	$4.3^{+1.1}_{-0.8} \times 10^{49}$
0.000	0.064	Comp	46 \pm 7	0.36 \pm 0.20	2820.00/517	0.063	$3.7^{+0.3}_{-0.3} \times 10^{48}$	$5.8^{+0.4}_{-0.5} \times 10^{49}$
0.064	0.200	Comp	21 \pm 8	0.68 \pm 0.64	369.18/180	0.190	$2.3^{+0.8}_{-0.2} \times 10^{48}$	$1.2^{+0.4}_{-0.1} \times 10^{49}$
-0.016	0.048	Comp	51 \pm 10	0.31 \pm 0.24	2444.00/386	0.063	$4.7^{+0.5}_{-0.4} \times 10^{48}$	$7.4^{+0.8}_{-0.7} \times 10^{49}$

Extended Data Table. 6: The parameters of GRB 211211A precursor QPO for different methods.

Method	Frequency (Hz) (GBM)	Frequency (Hz) (BAT)	GBM significance (σ)	BAT significance (σ)	GBM+BAT significance (σ)
weighted wavelet Z-transform	~ 22	~ 22	3.0	2.0	4.0
Lomb-Scargle Periodogram	21.9	21.6	-	-	-
fast fourier transform	22.5	22.5	4.1	3.0	5.4
auto-correlation	~ 22	~ 22	4.3	3.3	5.8
Z^2	23.5	21.8	7.3	3.9	8.5

Extended Data Table. 7: The parameters of GRB 211211A precursor FRED for *Fermi*/GBM, *Swift*/BAT, *Insight*-HXMT/HE, respectively.

	A	t_{max} (ms)	t_r (ms)	t_d (ms)	ν	B (cnts/s)
<i>Fermi</i> /GBM	18098.7 $^{+1949.6}_{-1636.7}$	-8.7 $^{+2.6}_{-2.2}$	8.0 $^{+2.4}_{-2.2}$	84.0 $^{+10.8}_{-10.7}$	1.0 $^{+0.1}_{-0.1}$	5501.5 $^{+38.5}_{-38.0}$
<i>Swift</i> /BAT	17105.0 $^{+1201.4}_{-1127.2}$	-6.3 $^{+2.6}_{-2.3}$	10.0 $^{+2.1}_{-2.2}$	99.2 $^{+8.0}_{-8.4}$	1.2 $^{+0.1}_{-0.1}$	3836.7 $^{+39.0}_{-39.5}$
<i>Insight</i> -HXMT/HE	3197.6 $^{+957.7}_{-623.9}$	-4.0 $^{+9.3}_{-5.6}$	10.4 $^{+12.2}_{-6.4}$	43.1 $^{+12.0}_{-12.3}$	2.3 $^{+3.0}_{-1.2}$	2643.8 $^{+31.0}_{-31.8}$